Coupled CFD/CSD Analysis of an Active-Twist Rotor in a Wind Tunnel with Experimental Validation

Steven J. Massey
Research Aerospace Engineer
NASA Langley Research Center
Hampton, VA

Andrew R. Kreshock
Research Aerospace Engineer
U.S. Army Research Laboratory
Hampton, VA

Martin K. Sekula
Research Aerospace Engineer
NASA Langley Research Center
Hampton, VA

ABSTRACT

An unsteady Reynolds averaged Navier-Stokes analysis loosely coupled with a comprehensive rotorcraft code is presented for a second-generation active-twist rotor. High fidelity Navier-Stokes results for three configurations: an isolated rotor, a rotor with fuselage, and a rotor with fuselage mounted in a wind tunnel, are compared to lifting-line theory based comprehensive rotorcraft code calculations and wind tunnel data. Results indicate that CFD/CSD predictions of flapwise bending moments are in good agreement with wind tunnel measurements for configurations with a fuselage, and that modeling the wind tunnel environment does not significantly enhance computed results. Actuated rotor results for the rotor with fuselage configuration are also validated for predictions of vibratory blade loads and fixed-system vibratory loads. Varying levels of agreement with wind tunnel measurements are observed for blade vibratory loads, depending on the load component (flap, lag, or torsion) and the harmonic being examined. Predicted trends in fixed-system vibratory loads are in good agreement with wind tunnel measurements.

NOTATION

Latin Symbols

C_p	coefficient of pressure
M	Mach number
M_β	flapwise bending moment, in-lb
M_θ	torsional bending moment, in-lb
M_ξ	chordwise bending moment, in-lb
Q	second invariant of the velocity gradient tensor
r	normalized rotor radius
U_{ref}	X-component of velocity at boundary layer edge ($0.995u_\infty$), ft/sec
u	X-component of velocity, ft/sec
X	axial CFD direction
y^+	dimensionless, sublayer-scaled wall coordinate of first node away from surface
Y	horizontal CFD direction, wall normal direction in boundary layer plots
Z	vertical CFD direction

Greek Symbols

δ	boundary layer thickness, Y for which $u = 0.995u_\infty$, in
δ^*	displacement thickness, $\int_0^\infty (1 - \frac{\rho u}{\rho_\infty u_\infty}) dY$, in
θ	momentum thickness, $\int_0^\infty \frac{\rho u}{\rho_\infty u_\infty}(1 - \frac{u}{u_\infty}) dY$, in
μ	advance ratio
ψ	azimuthal coordinate, deg

Subscripts

∞	free stream reference condition

Abbreviations

ARES	Aeroelastic Rotor Experimental System
ATR	Active-Twist Rotor
CAD	Computer-Aided Design
CAMRAD	Comprehensive Analytical Model of Rotorcraft Aerodynamics and Dynamics
CFD	Computational Fluid Dynamics
DiRTlib	Donor interpolation Receptor Transaction library
DOF	Degree of Freedom
EC	East Ceiling boundary layer rake location
EF	East Floor boundary layer rake location
EW	East Wall boundary layer rake location
FUN3D	Fully Unstructured Navier-Stokes 3-Dimensional
MFC	Macro-Fiber Composite
P	per revolution
CSD	Computational Structural Dynamics
SUGGAR	Structured, Unstructured, and Generalized overset Grid AssembleR
TDT	Transonic Dynamics Tunnel
UM/VABS	University of Michigan/Variational Asymptotic Beam Sectional
WC	West Ceiling boundary layer rake location
WF	West Floor boundary layer rake location
WW	West Wall boundary layer rake location

Presented at the AHS 71st Annual Forum, Virginia Beach, Virginia, May 5–7, 2015.

INTRODUCTION

An unsteady Reynolds averaged Navier-Stokes analysis coupled with a comprehensive rotorcraft structural dynamics code is presented for a second-generation Active-Twist Rotor (ATR) as tested in a wind tunnel, Figure 1. Analyses are performed for configurations of varying physical detail ranging from an isolated rotor to a rotor with a fuselage mounted

in a wind tunnel test section. Active twist technology creates a twist deformation using piezoelectric fiber composite actuators embedded in the skins of the blades, Figure 2. The actuators produce a shearing strain in the cross-section of a blade that incrementally changes the pitch angle along the length of the blade. This type of actuation, in effect, increases or decreases the built-in blade twist to change the airloads produced by the rotor.

The broad purpose of this study is to evaluate the accuracy of the present CFD/CSD model with and without active-twist actuation by comparing the results to measurements. Experimental data used for the validation of the coupled CFD/CSD model of the ATR examined in this study were obtained from wind tunnel tests (Ref. 1) conducted in NASA Langley's Transonic Dynamics Tunnel (Ref. 2). This study builds on a previous paper by the present authors (Ref. 3) that determined the mesh convergence requirements for a single configuration of the rotor with a fuselage over a range of flow conditions. In the present study, the influence of the fuselage as well as the influence of a wind tunnel is investigated by examining three CFD model configurations: an isolated rotor, a rotor with fuselage and a rotor with fuselage on a support stand installed in the wind tunnel, see Figure 3. It should be noted that the fuselage in the rotor with fuselage configuration, and the support structure in the rotor with fuselage mounted in the wind tunnel configuration do not change the fidelity of the structural model employed in this study. They are assumed to be rigid structures whose influence on the rotor response is limited to how their geometry changes the flow field.

The ATR concept has been studied, both numerically (Refs. 4, 5) and experimentally (Ref. 6), as a method to reduce vibratory loads, reduce rotor system noise, and improve performance through higher harmonic control and individual blade control. ATR blades generate dynamic twist during rotor operation by means of piezoelectric composite actuators embedded in the skin of the blade. The piezoelectric fibers are oriented at $\pm 45^{\circ}$ from the blade spanwise axis generating shear strains in the skin that induce twist in the blade. The first generation NASA/Army/MIT ATR blades used Active Fiber Composite (AFC) actuators, and were tested at the Transonic Dynamics Tunnel (TDT) at NASA Langley Research Center (Ref. 7). The ATR blades demonstrated sufficient twist authority to be able to minimize the primary vibratory loads induced by the rotor during flight. A set of second-generation active-twist rotor blades has been manufactured that provides greater control authority. This permits investigation of simultaneous active control methods to achieve multiple ATR objectives such as, vibratory load reduction, noise reduction, and rotor blade tracking. The ATR blades in this study use macro-fiber composite (MFC) piezoelectric actuators (Ref. 8). The MFCs in this application are actuated by a maximum of ± 500V generated by amplifiers in the non-rotating frame. Current is routed through a slip ring to each blade in the rotating frame.

The structural design of the ATR was determined using methodologies developed by Cesnic et al. (Ref. 9) and Thornburgh et al. (Ref. 10). The cross-sectional blade design identified through this process was analyzed using University of Michigan/Variational Asymptotic Beam Sectional (UM/VABS) computer code (Refs. 11, 12) to create a one-dimensional beam representation of the three-dimensional structure. The beam structural properties were then employed to develop the structural model of the rotor blades in the second generation version of the Comprehensive Analytical Model of Rotorcraft Aerodynamics and Dynamics (CAMRAD II) computer code (Ref. 13). To improve the aerodynamic modeling of this comprehensive analysis, CAMRAD II is coupled with the FUN3D CFD analysis (Ref. 14).

COMPUTATIONAL METHODOLOGY

In the following subsections, the methods and software components required to perform a multidisciplinary rotorcraft analysis are described in detail. The tools and methods used in this study follow those first implemented in FUN3D by Biedron and Lee-Rausch (Ref. 15).

CFD Mesh Generation

In our previous study (Ref. 3), which only examined the rotor with a fuselage configuration, meshes at three levels of refinement were evaluated over a range of flow conditions. Of the three meshes, the coarsest spacing was found to be sufficient and, therefore, is used here. As before, the meshes were constructed following the best practices published by Biedron and Lee-Rausch (Ref. 16) along with updates such as an increased farfield boundary extent to ten rotor radii when simulating free-air conditions.

The rotor blade mesh was created from the CAD definition used for the manufacturing of the wind tunnel test blades. The fuselage is modeled based on the current configuration of the Aeroelastic Rotor Experimental System (ARES) (Ref. 17) testbed. In the previous study, unstructured tetrahedral meshes were generated using VGRID (Ref. 18) with the input prepared using GridTool (Ref. 19). Tetrahedra in the boundary layer were merged into prisms using a utility program included in the FUN3D suite. For the new configurations in the present study, Pointwise^{TM} (Ref. 20) was used to create similar meshes as before. The blade mesh, which is shared by the three configurations examined in this study, was also regenerated with Pointwise^{TM}.

The rotor blade boundary layer was fully meshed with a first cell height of 1.5×10^{-5} inches corresponding to $y^{+} < 0.5$. All other viscous surfaces were set to 1.1×10^{-4} inches, which gives a $y^{+} \approx 0.8$ on most surfaces at the higher advance ratio condition. Node counts for the assembled meshes for the isolated rotor, rotor with fuselage, and rotor with fuselage mounted in the wind tunnel are 6.7, 5.9, and 12.6 million nodes respectively, with the rotor accounting for 4.6 million nodes in each case. Spanwise mesh spacing on the blade was 0.2 inches with 41 points distributed in the chordwise direction with clustering at the leading and trailing edges. As can be seen in Figure 3, the surface mesh on the fuselage mounted

in the wind tunnel is more uniform and finer, at a resolution of 0.5 inch, than the spacing on fuselage for the rotor with fuselage configuration, where the fuselage near the hub has a 0.63 inch spacing and double that on the main body. The higher resolution was maintained for the configuration in the wind tunnel so as to not preclude any aerodynamic influences that the support stand could impart to the rotor.

Finally, to validate the boundary layer prediction in the wind tunnel configuration, a fourth mesh was constructed of the empty TDT consisting of 4.0 million nodes. The computational domain for both TDT meshes is outlined in red in Figure 4. To more naturally model the inlet flow direction without modeling the turning vanes, a 12 ft extension was extruded from the inlet face. To improve CFD robustness at the exit, the domain was truncated at the downstream end of the splitter wall that houses the butterfly valve assembly.

The TDT is a slotted-throat tunnel. The slots are required to prevent choking at transonic Mach numbers and can also alleviate blockage effects in the high subsonic range, as first published by Wright and Ward (Ref. 21). For the low Mach numbers under consideration, the slots are not needed and therefore were not modeled. However, engineering practice at the TDT for non-acoustic rotorcraft tests is to leave the slots open with the reentry flaps closed. Unpublished comparisons with fully closed slots have shown that this tunnel configuration does not have any measurable effect on rotor performance measurements.

CFD Solver

Solutions to the Reynolds averaged Navier-Stokes (RANS) equations are computed using the FUN3D (Ref. 14) flow solver. All solid surfaces are modeled with no-slip boundary conditions. For the external flow cases, Riemann invariant farfield boundary conditions are used. For the wind tunnel cases, a fixed inflow boundary condition with the primitive variables specified is used. For the exit, the back pressure boundary condition is used, where the static pressure is specified, while velocity and temperature is extrapolated. Values for the inlet and exit parameters are calculated via isentropic relations to relate the conditions in the test section to the inlet and exit planes. As the computations progress, the back pressure is adjusted through interpolation to obtain the target test section Mach number. Turbulence closure is obtained using the Spalart-Allmaras (Ref. 22) one-equation model. Inviscid fluxes are computed using the Roe scheme (Ref. 23). For second-order spatial accuracy, interface values required for Roe's scheme are reconstructed using gradients at mesh nodes obtained by a least-squares technique. For the mixed prismatic/tetrahedral meshes used in this study the viscous fluxes are evaluated to second-order accuracy using a combination of edge-based and Green-Gauss gradients. In high gradient regions of the flow, limiters on these reconstructed values may be needed for stability. However, in the present computations, no limiters were required.

Time integration is accomplished by an Euler implicit backwards difference scheme with dual time stepping to achieve second-order accuracy (Refs. 24, 25). Following best practices, time accurate solutions were generated using at least 25 subiterations. The only case to require more subiterations was that of the rotor with fuselage mounted in the wind tunnel at $\mu = 0.13$, where in order to maintain numerical stability, 50 subiterations were required for the first trim cycle, followed by 100 subiterations for trim cycles, 2-7, and finally 200 subiterations for cycles 8 and 9. To quickly establish the tunnel flow, the rotor with fuselage mounted in the wind tunnel cases are initialized in three stages while monitoring the Mach number one rotor diameter upstream of the rotor hub, namely: 1) run first order accuracy in space and time with a large time step that covers 10° of rotor rotation or 36 steps per revolution until Mach number becomes asymptotic (approximately 2000 steps); 2) increase to second order accuracy in space until the Mach number becomes asymptotic again (approximately 1500 steps), adjust back pressure as needed and repeat step 2; 3) increase to second order accuracy in time with at least 25 subiterations with a time step that limits the rotor motion to 1° per step for at least 720 steps. At this point the CFD/CSD trim convergence cycling can begin. This procedure is summarized on a plot of the Mach number history in Figure 5.

Mesh motion due to blade deformations is carried out by treating the CFD mesh as a linear elastic medium with material properties based on the mesh characteristics with appropriate application of the Geometric Conservation Law (Ref. 26). Rotor motion is handled by means of an overset mesh methodology, which is implemented in FUN3D via the Donor interpolation Receptor Transaction library (DiRTlib) (Ref. 27) and the Structured, Unstructured, and Generalized overset Grid AssembleR (SUGGAR) (Ref. 28).

CSD Solver

In the present study, CAMRAD II (Ref. 13) is used to predict the dynamic behavior of the ATR. CAMRAD II is a rotorcraft-centric aeromechanical analysis tool that combines a multibody dynamics formulation with nonlinear finite elements to model rotorcraft structures: rotors, control systems, fuselage, and various aerodynamic surfaces. Active-twist actuation is modeled as a torsional moment couple that is placed at the inboard and outboard bounds of the active region of a beam-model representation of the blade. This torsion moment couple creates a spanwise constant torsion moment across the active region highlighted in Figure 2. The structural properties of the beam model and torsion moment magnitude are calculated using UM/VABS. UM/VABS converts a detailed cross-sectional model of a rotor blade into beam properties. UM/VABS also converts the strain-induced twist-per-length produced from the embedded piezoelectric actuators into a beam torsion moment required to simulate active-twist.

CAMRAD II incorporates a lifting line model to determine the rotor aerodynamic loads, with a customizable wake model ranging in complexity from a simple linear inflow to a deforming free wake. Because the aerodynamic models within CAMRAD II are based on lifting-line theory coupled with airfoil

tables and wake models, higher fidelity Navier-Stokes aerodynamics are imported into CAMRAD II via a loose coupling procedure first suggested by Tung et al. (Ref. 29) and implemented in FUN3D by Biedron and Lee-Rausch (Ref. 15). In the present study, airloads data from the CFD solver and blade motion data from the CSD solver are exchanged at periodic intervals of twice per revolution.

CFD/CSD Coupling Details

The loads from the CFD solution are transferred to the CSD code through an intermediate code (Ref. 30). The CFD code calculates the sectional loads along the blade. The intermediary code takes the differential load between the CFD and the CSD solvers and interpolates it to locations that correspond with the CSD model's aerodynamic panels. A new differential load is then applied to the CSD model for every coupling cycle until convergence is established. Convergence is determined by monitoring the rotor controls, rotor thrust and torque. To complete the coupling cycle after the CSD code has trimmed to a new solution, the motion differential, due to the updated loads, is transferred back to the CFD code, which then applies the new rotor motion and mesh deformations to the CFD domain.

CAMRAD II Rotor Model

The ATR is a 4-bladed, articulated, 10.56-foot diameter rotor with a solidity of 0.0928 and includes a 20° swept tip over the outer seven percent of the rotor radius. The structural model consists of three radial sections: (1) rigid hub, (2) rigid section of the blade and cuff, and (3) elastic blade. The inboard-most section represents the rotor hub and is approximated by a rigid beam element. The two sections outboard of the hub represent the rotor blades. The inner section is modeled by three rigid elements representing (1) the structure between the flap-lag hinges and blade pitch bearing, (2) the blade cuff, and (3) the inboard section of the actual rotor blade, which is made of solid fiberglass to provide a reliable interface with the cuff. Mass and inertial properties were determined by experiment and CAD analysis. The rotor blade is modeled using eleven elastic beam elements, each having elastic flap, lag, torsion, and extensional degrees of freedom. The accuracy of the blade structural model was confirmed through bench testing to determine natural frequencies and deflections due to applied loads.

Two of CAMRAD II's internal aerodynamic models are employed in this study. The first is a free wake model. The deformable, single peak wake extends two rotor revolutions behind the rotor blades, and is used with a 25-panel lifting-line model to develop the blade aerodynamic loads. The second is a uniform inflow model employing a 96-panel lifting line analysis. This aerodynamic model is used as part of the coupling process with the CFD solver, which exports its aerodynamic loads at 200 radial stations along the blade. The aerodynamic and structural models result in a large number of equations of motion, therefore a modal reduction, using 10 blade modes, is used to reduce the number of degrees of freedom in the model. The resulting blade equations of motion are solved using a harmonic balance method. The four rotor blades are assumed to be identical; therefore the equations of motion are solved for a single blade. The phase of the solution is adjusted for each rotor blade, and the loads of all the blades are summed to produce the rotor loads.

Rotor trim is determined by a Newton-Raphson approach. The control inputs are the rotor collective pitch, lateral cyclic pitch, and longitudinal cyclic pitch, which are used to eliminate 1/rev blade flapping while providing a specified rotor thrust. The rotor shaft tilt is specified to match experimental shaft tilt, instead of being included as a variable in the trim solution. This approach was applied to both the free wake and the coupled CFD/CSD solution for consistency, since the methodology behind the CFD/CSD solution requires the rotor shaft angle to remain constant.

EMPTY WIND TUNNEL BOUNDARY LAYER VALIDATION

Before beginning the simulation of the rotor with fuselage mounted in the wind tunnel, it was first necessary to validate the CFD approach. Two important characteristics of the tunnel flow field are the boundary layer thickness and its variation along the circumference of the test section. Therefore, a validation case was constructed as closely as possible to the higher advance ratio case, which corresponded to run point 1221 from Ref. 31 - heavy gas test medium with a test section Mach number of 0.2 and slots open. A more complete validation study over a wide range of flow conditions, including the throat slots, reentry flaps and their associated plenum is beyond the scope of this study, but is currently underway.

Six boundary layer rakes were located at the 72 ft station in the coordinate system of the test report (Ref. 31). The positions are shown in blue in Figure 6. The cutting plane mesh is also shown in green for inside the boundary layer and red for the outside, as defined by the threshold of $u = 0.995u_\infty$. For orientation, this plane is shown inside the full CFD wind tunnel domain in Figure 7. From the rake data, the boundary layer thickness, displacement thickness and momentum thickness were computed and tabulated in Table 1. Due to the relatively low dynamic pressure at this test point, there is considerable scatter in some of the measurements due to the sensitivity limitations of the pressure transducers. This scatter makes it difficult to calculate boundary layer thickness accurately, therefore the values for this parameter were extrapolated from the Mach 0.3 condition in Figure 17 of (Ref. 31). All other quantities were computed from the velocity profile data plotted in Figure 8. Overall, the agreement in the boundary layer thickness is very good, with the exception of the east wall and which is double that of the FUN3D prediction as well as four of the other measured locations. It is worth noting that an earlier test (Ref. 32) reported a boundary layer thickness on the east wall of only 36% of the value in (Ref. 31) for air at M=0.6. However, FUN3D does predict a 22% increase in the boundary layer thickness relative to the east floor at this point.

With regard to the circumferential variation of the boundary layer thickness, FUN3D shows a gradual thickening moving from west to east, while TDT data shows a thick boundary layer on the west side of the floor and the east wall.

EFFECT OF CONFIGURATION ON UNACTUATED ROTOR BLADE BENDING MOMENTS

In this section, configuration effects are investigated for an unactuated rotor. The three configurations consist of an isolated rotor, a rotor with fuselage, and a rotor with fuselage mounted in the TDT, shown in Figure 3. The rotor with fuselage configuration, Figure 3(b), was previously studied at two advance ratios by the present authors (Ref. 3), to determine the mesh convergence requirements and accuracy compared to a lower-fidelity CAMRAD II free wake model and wind tunnel measurements. Results are presented for the same advance ratios, namely, $\mu = 0.13$ and $\mu = 0.33$, but the study has been expanded to three CFD/CSD configurations (using an updated blade geometry) and compared to wind tunnel measurements and CAMRAD II free wake model results. Results are also presented for CAMRAD II as a stand-alone comprehensive solver to highlight where CFD provides the most benefit, since coupling with CFD is at least three orders of magnitude more computationally expensive.

The trim solutions for the experiment and the various analytical models are presented in Tables 2 and 3 for advance ratios of 0.13 and 0.33, respectively. The tables indicate that model configuration (isolated rotor, rotor with fuselage, or rotor with fuselage mounted in the TDT) as well as the aerodynamic model (CFD vs. free wake model) significantly affect the rotor trim. None of the analytical models predict the trimmed control setting correctly. The control setting for the lowest fidelity model, the free wake model, displays the largest differences from the experimental values. In general, the computed longitudinal cyclic pitch settings were the closest to the experimental values, while the collective pitch predictions were worst. Increasing the fidelity of the coupled CFD/CSD model (i.e., adding the fuselage and wind tunnel) did not improve the control settings predictions.

Before analyzing the rotor blade bending moments it is instructive to notice the similarity in wake vortical structure for the three configurations studied, Figure 3. One readily apparent difference between the configurations is the wake of the hub, which is significant because it intersects with the rotor plane. In the present study, the hub is non-rotating, however, given the size of the wake, it may be important to model this region more accurately in the future. Also apparent is the rotor wake tip vortex coming from the retreating blade seems to be positioned lower in the isolated rotor case than the other configurations due to upwash from the fuselage, which will certainly affect blade loading. It is encouraging to see that the fuselage support structure does not appear to affect the aerodynamics in the rotor plane. It does, however, impart a strong vortex at the base of the fuselage due to the gap between the airfoil shaped shroud and the fuselage. Horizontal and vertical cut planes of Mach number in the wind tunnel for both advance ratios, Figures 9 and 10, indicate that the flow is very uniform entering the test section and that there appears to be sufficient separation between the tunnel walls and the rotor flow field. Note that the vertical cut plane appears shorter due to the presence of the splitter wall.

Trim and mesh converged values of flapwise, torsional, and chordwise bending moments are plotted together with wind tunnel measurements and CAMRAD-II free wake results at three radial stations in Figures 11. As observed in the previous study (Ref. 3), flapwise moments are most accurately predicted and CAMRAD II free wake model does well at the low advance ratio, but is not as accurate as the coupled CFD/CSD solutions at the higher advance ratio. At the lower advance ratio, the rotor with fuselage mounted in the wind tunnel configuration shows more of a departure from the other solutions (but not consistently closer to the measurements), perhaps due to an increased interaction of the rotor wake and the tunnel boundary for the very low tunnel Mach number of 0.08 ($\mu = 0.13$). For the higher advance ratio case, the isolated rotor CFD/CSD case is seen to be markedly different from the two rotor cases that include the fuselage, while the addition of the wind tunnel test section and support structure made very little difference. Thus, it is concluded that at the higher advance ratio the presence of the fuselage is significantly more important than the modeling of the surrounding wind tunnel environment. The converse is true at low advance ratios.

Wind tunnel measurements of flapwise bending moment are plotted along with computational results for advance ratios $\mu = 0.13$ and $\mu = 0.33$ in Figures 12 and 13, respectively. For the low advance ratio case, shown in Figure 12, all of the computations including the low fidelity CAMRAD II free wake model are in fairly good agreement with test data. The isolated rotor CFD/CSD case, Figure 12(c), shows slightly reduced values for the peaks at azimuth angles of 285° and 350° compared to the rotor with the fuselage case, Figure 12(d), while the rotor with fuselage mounted in the wind tunnel case, Figure 12(e), more closely matches measurements in those areas, Figure 12(a).

In the higher advance ratio case results, Figure 13, the CAMRAD II free wake results, Figure 13(b), are very similar to the isolated rotor CFD/CSD case, Figure 13(c), with the exception of the area near $\psi = 90°$, where the free wake case more closely matches data. This similarity may be due to the fact that the CAMRAD II free wake model is inherently an isolated rotor. Unlike the lower advance ratio case though, both isolated rotor cases significantly under predict the amplitudes of the bending moment extremes while the two CFD/CSD solutions that include a fuselage over predict the radial and azimuthal extent of the high flapwise bending moment regions, which occur at approximately 190° and 270°. Overall there is very little difference between the the flapwise bending moment distributions for the rotor and fuselage case, Figure 13(d), verses its inclusion in the wind tunnel, Figure 13(e). Thus, it is concluded that there are no aerodynamic

artifacts from the ARES support stand or the wind tunnel that significantly affect flapwise bending moments at these conditions. Therefore, differences between the computed results and measurements can not be attributed to the wind tunnel environment.

Contour plots of the rotor disk depicting the torsional and chordwise moments are presented in Figures 14 through 17. These plots do not include wind tunnel results due to the lack of sensor data. As with the flapwise results, the CAMRAD II free wake model is comparable to CFD/CSD for the low advance ratio case results, Figures 14 and 16. At the higher advance ratio, the torsional bending moments predicted by the CAMRAD II free wake model, Figure 15(a), differ from the CFD/CSD cases. The free wake model predicts that the maximum negative torsion moment occurs at approximately the 130° azimuth location, while the CFD/CSD cases predict that it occurs at 270°, see Figure 15. Inclusion of the fuselage in the CFD/CSD cases increased the magnitude of the negative bending moment near 270° azimuth. As with the flapwise bending moment, the torsional bending moment results differ very little between the rotor with fuselage case, Figure 15(c), and the rotor with fuselage installed in the TDT, Figure 15(d). This observation is also noted for the chordwise bending moments, Figures Figures 17(c) and 17(d).

Of all the distributed moment plots, the effect of the isolated rotor is most apparent in the plot of chordwise bending moment for the higher advance ratio, Figures 17. In this plot, the CAMRAD II free wake results, Figure 17(a), match very well with the isolated rotor CFD/CSD prediction, Figure 17(b), where both predict a much lower amplitude compared to the cases that include the fuselage, particularly near $\psi = 240°$. Examining the experimental chordwise bending moment time history at $r = 0.2$, Figure 11(f), it would appear that the lower amplitude is more correct in this case.

ACTIVE-TWIST RESULTS FOR ROTOR WITH FUSELAGE CONFIGURATION

The underlying concept behind active rotors is the ability to adjust aerodynamic loads produced by the rotor to address any number of persistent rotorcraft problems such as noise or vibratory loads. The ATR is a four bladed rotor, therefore to affect fixed-system vibratory loads, actuation at frequencies of 3P, 4P, and 5P is employed.

Active twist actuation requires three inputs: amplitude, frequency, and phase. The effects of these control inputs on the blade loads are presented using response maps where each plot presents the sine and cosine components of a specific harmonic of the blade loads. Figures 18 and 19 compare the 3P, 4P, and 5P blade loads measured during the wind tunnel test and the rotor with fuselage CFD/CSD analysis at an advance ratio of 0.125. For these two cases, voltage excitation of 500 V amplitude was employed at an actuation frequency of 3P and 4P, respectively. The phase of the actuation was changed in 20° increments resulting in the circular pattern of the response plot. Where possible, radial lines are shown to indicate the response generated when applying 0° control phase. For all cases, the control phase advances counterclockwise around the plotted data. The unactuated case (filled symbol) in the center of the response plot consists of a trimmed CFD/CSD analysis described earlier. Each active-twist CFD/CSD result (open red squares) represents an untrimmed CFD/CSD analysis consisting of five coupling cycles using the trimmed rotor control settings (cyclic and collective pitch) from the unactuated case. This approach is analogous to the experimental procedure, where the unactuated rotor is trimmed and then the active controls are varied while the rotor controls are held constant.

The 3P actuation results, presented in Figure 18, indicate that the primary effect on the blade loads occurs at the third harmonic. There is only a limited effect of 3P active-twist on the 4th and 5th harmonics of the blade loads, although the analytical model indicates more sensitivity of the 4th and 5th harmonics to the 3P actuation than seen in the experimental results. The 3P flapwise bending moment, Figure 18(a), indicates good agreement in the change of load magnitude due to active-twist actuation. The actuated rotor results indicate a 10° offset in the actuation phase of the analytical results with respect to the experimental data. This offset may be explained in part by a documented hysteresis in the strain-voltage relationship exhibited by the MFCs (Ref. 1). The worst discrepancy in blade load prediction occurs in the chordwise blade bending moment. The analytical model indicates significant sensitivity to 3P active-twist actuation, which is lacking in the experimental data. This observation agrees with previous discussion of chordwise bending moment results in Figures 11 and 17.

A full phase sweep for the 4P actuation was not conducted during wind tunnel testing to avoid exceeding the fixed-system load limits of the test article, see Figure 19. The torsion response due to 4P actuation is well predicted for the 3rd and 4th harmonic, see Figures 19(d) and 19(e), while the 5th is overpredicted. The 4P component is the largest because this load includes the control input moment that induces the twist change. The 3P and 4P torsion moment response plots both indicate a 10° difference in the active-twist control phase, while the 5P torsion response plot control phase difference is much larger. The flapwise bending moment response, Figures 19(a)-19(c), also shows good agreement between analytical models and experimental data. The 4P flapwise bending moment appears to have the best comparison with respect to the change in response plot magnitude due to 4P active-twist actuation. The change in the 3P flapwise moment response of the analytical model is over predicted by approximately 40%. Both the 3P and 4P response plots indicate an approximate 20° control phase change between the analytical and experimental results. The analytically predicted 5P flapwise bending moment response plot due to 4P actuation exhibits an oblong shape instead of being circular like the lower harmonics. A similar deviation from the circular nature of the response plot is also observed in the limited experimental results, see Figure 19(c). The chordwise blade bending moment response due to 4P active-twist actuation is presented

in Figures 19(g)-19(i). The analytical model 3P chordwise bending moment response due to active-twist control is significantly over predicted, and the unactuated load prediction is also significantly off. The analytical 4P and 5P response appears to compare somewhat more reasonably with the experimental results, compared to the 3P response, but the comparisons are still not adequate. The observation that the 3P chordwise response is so significantly over predicted for both 3P and 4P actuation, coupled with the fact that experimental frequency response functions indicate very limited chordwise response below 3P (not presented), suggest the potential for a lower-frequency mode in the analytical model having an overstated chordwise component. This possibility indicates that the blade structural model may need further improvement.

Figure 20 presents the percent change of the baseline 4P fixed-system loads as a function of actuation phase. These plots compare experimental and analytical results for 3P actuation at an advance ratio of 0.125 and 500 V excitation voltage. The experimental results are represented by black circles while the analytical results are represented by red squares. Positive change in the plots indicates an increase in vibration relative to the baseline (unactuated) loads; conversely, a negative change indicates a vibration reduction. The experimentally-measured fixed-system loads were measured by a 6-DOF balance located approximately 20 inches below the rotor on an elastic testbed, while the analytical model loads were determined at the rotor hub. Also, the analytical model lacks a structural model of the testbed, and testbed dynamics can significantly impact the magnitude of the measured and computed loads. In light of these fundamental differences between experiment and analysis, examining trends in the vibratory data is more appropriate than direct comparisons of the fixed-system vibratory loads.

In general, Figure 20 indicates that there is good comparison between experimental and analytical trends in how active-twist actuation affects the fixed-system 4P vibratory loads at this test condition (μ=0.125). The percent change in the vibratory loads and the actuation phase at which loads are increased and reduced match extremely well for axial and side forces, Figures 20(a) and 20(b), and for rolling, pitching, and yawing moments, Figures 20(d)-20(f). Both experiment and analysis indicate a significant fixed-system load reduction between 200° and 250° actuation phase. The largest vibration reduction for all six fixed-system loads appears to occur at 220° actuation phase, resulting in vibration reductions of 58%, 77%, 58%, 81%, 58%, and 44% for axial, side, normal, roll, pitch, and yaw loads, respectively. The analytical model predicts a vibration reduction of 75%, 87%, 3%, 73%, 69%, and 59% for the same loads at the same actuation phase. The worst comparison occurs for the normal hub force, Figure 20(c). There is a phase shift in the trend of how the vibratory load is affected by the actuation phase and the vibratory load reduction noted in the experimental data is significantly under predicted by the analytical model.

CONCLUSIONS

A coupled CFD/CSD analysis was conducted on the second generation Active Twist Rotor using three CFD configurations of varying complexity: an isolated rotor, a rotor with a fuselage, and a rotor with a fuselage mounted in a wind tunnel. The unactuated and actuated results were compared to experiment and a low-fidelity free wake model resulting in the following conclusions:

1. A FUN3D RANS simulation on an unstructured mesh of only 4 million nodes was able to accurately capture the boundary layer profile of the TDT at a low subsonic condition.

2. CFD results indicate that for the conditions in the study, the flow field in the test section is very uniform and there is sufficient separation between the walls and the rotor flow field.

3. Flapwise bending moments were most accurately predicted by the coupled CFD/CSD cases, which included the fuselage, followed by torsional moments and chordwise moments.

4. Modeling the fuselage is more important than the modeling of the wind tunnel at the higher advance ratio.

5. At the lower advance ratio, modeling of the wind tunnel environment does affect the computed bending moments, but does not entirely account for the differences between computations and measurements for the torsional and chordwise results.

6. The best agreement between experimental and analytical blade loads due to active-twist actuation were for the 3P and 4P flapwise and torsion moments.

7. The CFD/CSD predicted trends in fixed-system vibratory load reduction due to 3P actuation were in good agreement with wind tunnel measurements.

Author contacts

Steven.J.Massey@nasa.gov
Andrew.R.Kreshock@nasa.gov
Martin.K.Sekula@nasa.gov

ACKNOWLEDGMENTS

The authors gratefully acknowledge Pawel Chwalowski for many fruitful discussions regarding his modeling of the TDT and his assistance in developing the mesh for the TDT. Also, Carol Wieseman for providing TDT boundary layer data.

REFERENCES

[1]Kreshock, A. R., *Design, Analysis and Testing of Active Twist Rotor Blades*, Master's thesis, Old Dominion University, Norfolk, VA, 2013.

[2]William T. Yeager, J. and Kvaternik, R. G., "A Historical Overview of Aeroelasticity Branch and Transonic Dynamics Tunnel Contributions to Rotorcraft Technology and Development," NASA TM 2001–211054, August 2001.

[3]Massey, S. J., Kreshock, A. R., and Sekula, M. K., "Coupled CFD/CSD Analysis of Rotor Blade Structural Loads with Experimental Validation," Paper 2013–3158, 31st AIAA Applied Aerodynamics Conference Proceedings, June 2013.

[4]Booth, E. R. and Wilbur, M. L., "Acoustic Aspects of Active-Twist Rotor Control," *Journal of the American Helicopter Society*, Vol. 49, (1), January 2004, pp. 3–10.
doi: 10.4050/JAHS.49.3

[5]Fogarty, D. E., Wilbur, M. L., and Sekula, M. K., "A Computational Study of BVI Noise Reduction Using Active Twist Control," American Helicopter Society 66th Annual Forum Proceedings, May 2010.

[6]Bernhard, A. P. F. and Wong, J., "Wind-Tunnel Evaluation of a Sikorsky Active Rotor Controller Implemented on the NASA/Army/MIT Active Twist Rotor," American Helicopter Society 59th Annual Forum Proceedings, May 2003.

[7]Wilbur, M. L., Mirick, P. H., Yeager, W. T., Langston, C. W., Cesnick, C. E. S., and Shin, S., "Vibratory Loads Reduction Testing of the NASA/Army/MIT Active Twist Rotor," American Helicopter Society 57th Annual Forum Proceedings, May 2001.

[8]Wilkie, W. K., Bryant, R. G., High, J. W., Fox, R. L., Ileilbaum, R. F., Jalink, A., Little, B. D., and Mirick, P. H., "Low-Cost Piezocomposite Actuator for Structural Control Applications," SPIE 7th Annual International Symposium on Smart Structures and Materials, 2000.

[9]Cesnik, C., Mok, J., Morillo, J., and Parikh, A., "Design Optimization of Active Twist Rotor Blades," European Rotorcraft Forum, 2004.

[10]Thornburgh, R., Kreshock, A., and Wilbur, M., "Structural Optimization of Active-Twist Rotor Blades," American Helicopter Society 67th Annual Forum Proceedings, 2011.

[11]Cesnik, C. E. S. and Hodges, D. H., "VABS: A New Concept for Composite Rotor Blade Cross-Sectional Modeling," *Journal of the American Helicopter Society*, Vol. 42, (1), 1997, pp. 27–38.

[12]Palacios, R. and Cesnik, C. E. S., "Cross-Sectional Analysis of Non-Homogeneous Anisotropic Active Slender Structures," *AIAA Journal*, Vol. 43, (12), 2005, pp. 2624–2638.

[13]Johnson Aeronautics, Palo Alto, CA, *Comprehensive Analytical Model of Rotorcraft Aerodynamics and Dynamics II v4.6*, 2007.

[14]Biedron, R. T., Derlaga, J. M., Gnoffo, P. A., Hammond, D. P., Jones, W. T., Kleb, B., Lee-Rausch, E. M., Nielsen, E. J., Park, M. A., Rumsey, C. L., Thomas, J. L., and Wood, W. A., "FUN3D Manual: 12.5," NASA TM 2014-218520, September 2014.

[15]Biedron, R. T. and Lee-Rausch, E. M., "Rotor Airloads Prediction Using Unstructured Meshes and Loose CFD/CSD Coupling," AIAA Paper 2008-7341, August 2008.

[16]Biedron, R. T. and Lee-Rausch, E. M., "Computation of UH-60A Airloads Using CFD/CSD Coupling On Unstructured Meshes," American Helicopter Society 67th Annual Forum Proceedings, May 2011.

[17]Yeager, W. T., Wilbur, M. L., and Nixon, M. W., "A Review of Recent Rotorcraft Investigations in the Langley Transonic Dynamics Tunnel," AIAA Paper 2003-1963, 2003.

[18]Pirzadeh, S. Z., "Advanced Unstructured Grid Generation for Complex Aerodynamic Applications," AIAA Paper 2008–7178, August 2008.

[19]Samareh, J. A., "Unstructured Grids on NURBS Surfaces," AIAA Paper 1993–3454, August 1993.

[20]Pointwise, Inc., Fort Worth, Texas, *Pointwise User Manual*, 2014.

[21]Wright, R. H. and Ward, V. G., "NACA Transonic Wind-Tunnel Test Sections," NACA RM L8J06, October 1948.

[22]Spalart, P. R. and Allmaras, S. R., "A One-Equation Turbulence Model for Aerodynamic Flows," *La Recherche Aerospatiale*, No. 1, 1994, pp. 5–21.

[23]Roe, P. L., "Approximate Riemann Solvers, Parameter Vectors, and Difference Schemes," *Journal of Computational Physics*, Vol. 43, 1981, pp. 357–372.

[24]Nyukhtikov, M., Smelova, N., Mitchell, B. E., and Holmes, D. G., "Optimized Dual-Time Stepping Technique For Time-Accurate Navier-Stokes Calculation," Proceedings of the 10th International Symposium on Unsteady Aerodynamics, Aeroacoustics and Aeroelasticity of Turbomachines, 2003.

[25]Vatsa, V. N., Carpenter, M. H., and Lockard, D. P., "Re-evaluation of an Optimized Second Order Backward Difference (BDF2OPT) Scheme for Unsteady Flow Applications," AIAA Paper 2010–0122, January 2010.

[26]Thomas, P. D. and Lombard, C. K., "Geometrical Conservation Law and Its Application," *AIAA Journal*, Vol. 17, (10), October 1978, pp. 1030–1037.

[27]Noack, R. W., "DiRTlib: A Library to Add an Overset Capability to Your Flow Solver," AIAA Paper 2005-5116, June 2005.

[28]Noack, R. W., "SUGGAR: a General Capability for Moving Body Overset Grid Assembly," AIAA Paper 2005-5117, June 2005.

[29]Tung, C., Caradonna, F., and Johnson, W., "The Prediction of Transonic Flows on an Advancing Rotor," American Helicopter Society 40th Annual Forum Proceedings, May 1984.

[30]D. Douglas Boyd, J., "HART-II Acoustic Predictions using a Coupled CFD/CSD Method," American Helicopter Society 65th Annual Forum Proceedings, May 2009.

[31]Wieseman, C. D. and Bennett, R. M., "Wall Boundary Layer Measurements for the NASA Langley Transonic Dynamics Tunnel," NASA TM 2007–214867, April 2007.

[32]Staff of the Aeroelasticity Branch, "The Langley Transonic Dynamics Tunnel," LWP–799, September 1969.

Table 1. Measured and FUN3D boundary layer thicknesses in the TDT.

	δ, inches		δ^*, inches		θ, inches	
Point	Measured[a]	FUN3D	Measured	FUN3D	Measured	FUN3D
EC	7.5	6.0	0.46	0.28	0.40	0.24
EW	14.0	7.3	0.54	0.32	0.45	0.27
EF	7.0	6.0	0.47	0.28	0.40	0.24
WC	7.5	5.9	0.46	0.27	0.40	0.23
WW	6.0	5.6	0.42	0.25	0.37	0.21
WF	10.0	5.9	0.51	0.27	0.43	0.23

[a] Measured δ were extrapolated from M=0.3 in Figure 17 of (Ref. 31).

Table 2. Measured and computed trim settings for $\mu = 0.13$.

Configuration	Collective, deg	Lateral Cyclic, deg	Longitudinal Cyclic, deg
Measured	7.1	-2.9	2.0
CAMRAD Free Wake	8.3	-2.5	2.4
Isolated Rotor CFD/CSD	7.1	-2.9	2.2
Rotor + Fuselage CFD/CSD	7.0	-3.1	2.3
Rotor + Fuselage in TDT CFD/CSD	6.4	-2.7	2.2

Table 3. Measured and computed trim settings for $\mu = 0.33$.

Configuration	Collective, deg	Lateral Cyclic, deg	Longitudinal Cyclic, deg
Measured	12.5	-3.2	7.1
CAMRAD Free Wake	13.6	-2.0	7.0
Isolated Rotor CFD/CSD	12.0	-2.5	7.1
Rotor + Fuselage CFD/CSD	11.8	-2.9	7.1
Rotor + Fuselage in TDT CFD/CSD	11.5	-3.0	7.0

Fig. 1. ARES/ATR model in the Transonic Dynamics Tunnel (TDT).

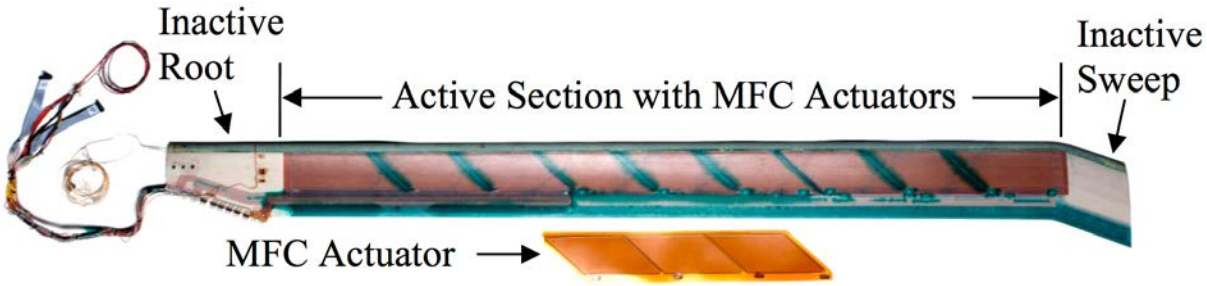

Fig. 2. Active-Twist Rotor blade with embedded actuators and supporting wiring for actuation and on-blade sensors.

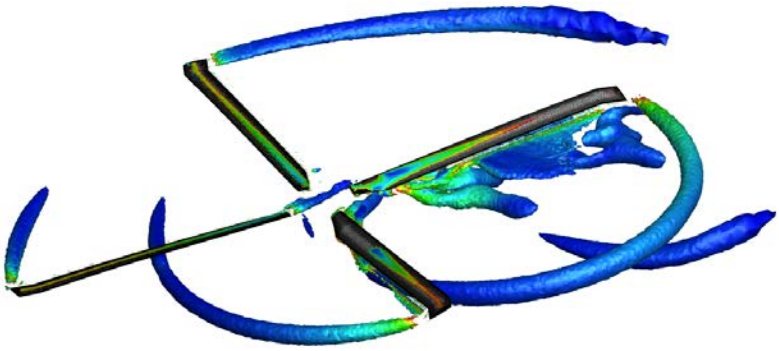

(a) Isolated rotor.

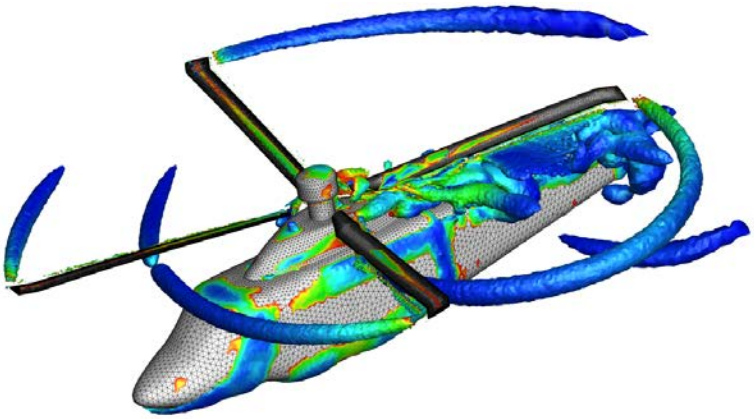

(b) Rotor with fuselage.

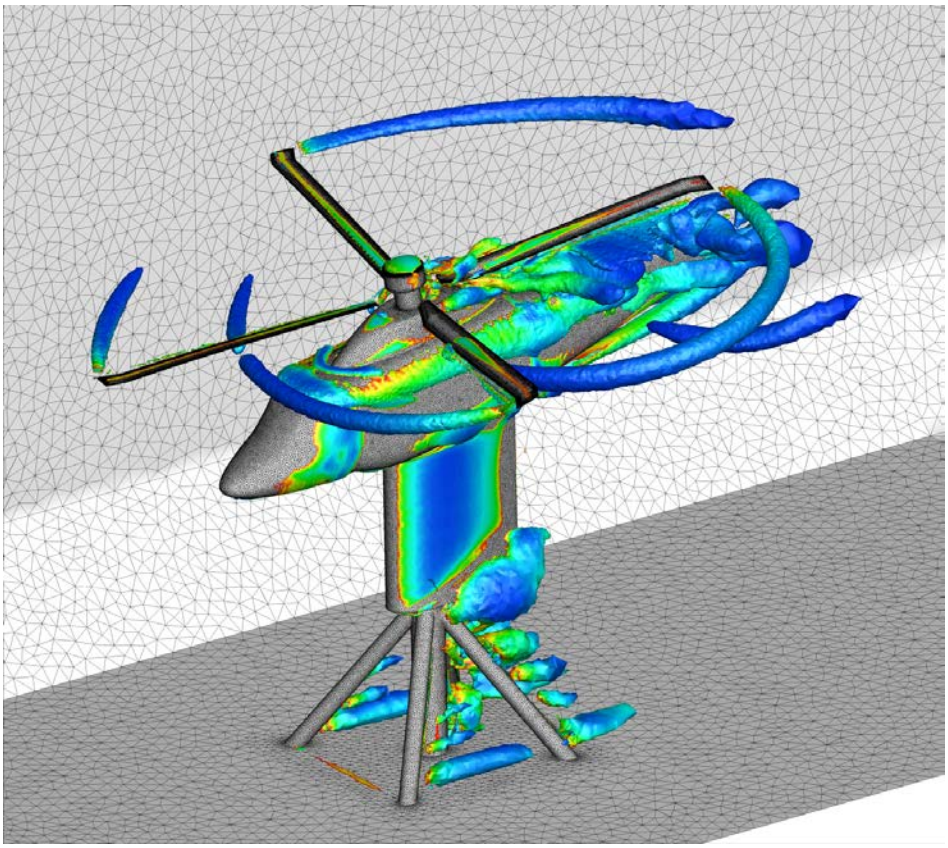

(c) Rotor with fuselage mounted in the TDT.

Fig. 3. Surface meshes and isosurfaces of Q=0.00005 colored by vorticity magnitude for the three configurations simulated, μ=0.33.

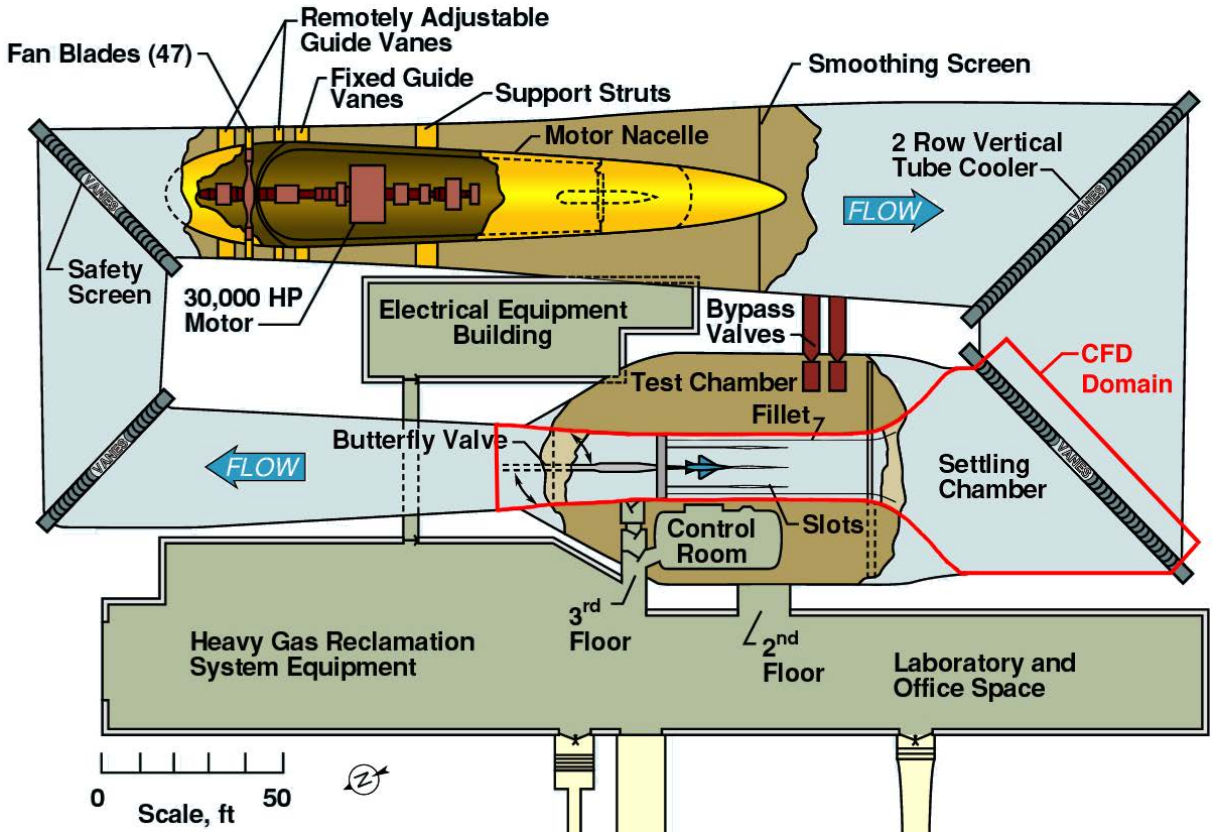

Fig. 4. Plan view of the TDT with the CFD domain shown in red.

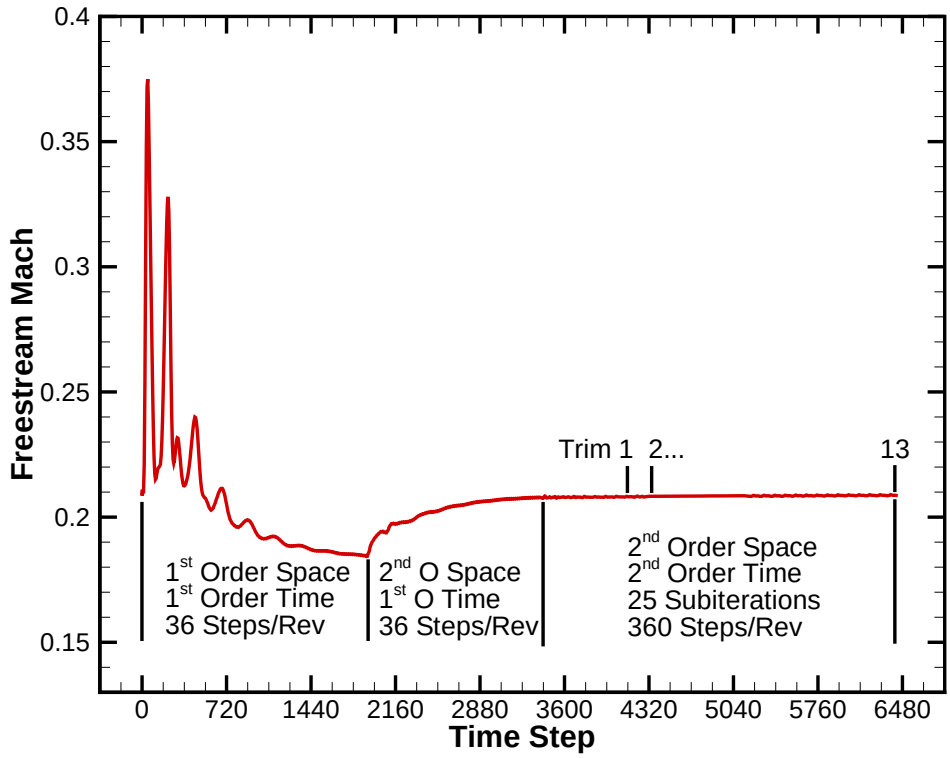

Fig. 5. Mach history along the tunnel centerline one rotor diameter upstream of the hub with the flow initialization procedure for FUN3D/CAMRAD II computations in the TDT for M=0.21, μ=0.33 case.

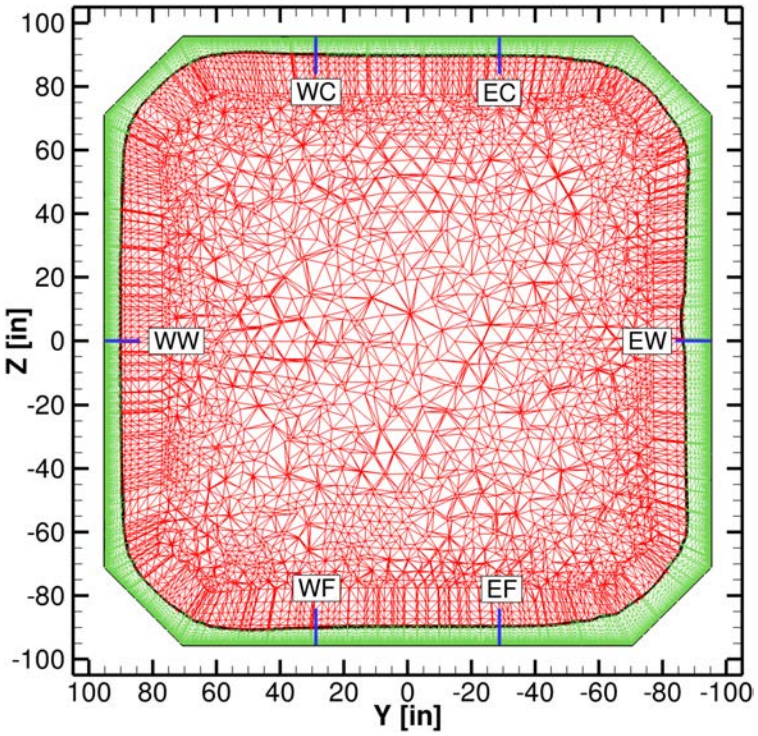

Fig. 6. Boundary layer sampling locations on the X=72 ft station, as measured in (Ref. 31). Rake locations shown in blue with the mesh inside the boundary layer colored green and outside red.

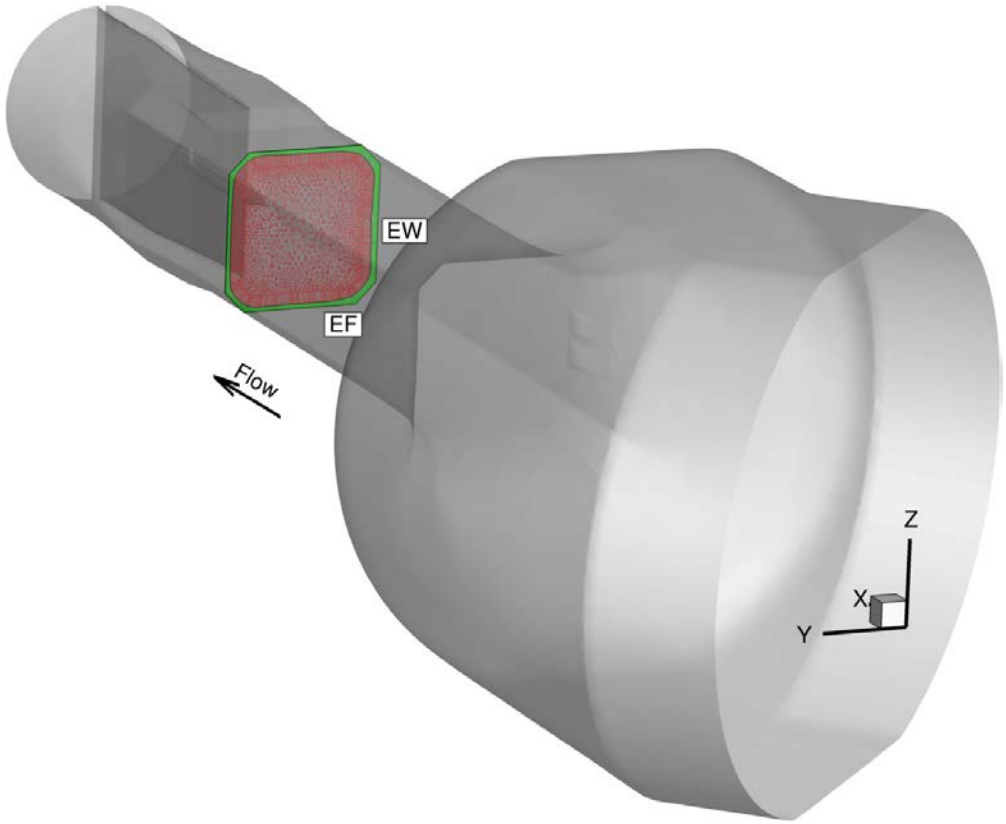

Fig. 7. Orientation of the boundary layer sampling plane within the computational domain of the empty TDT case.

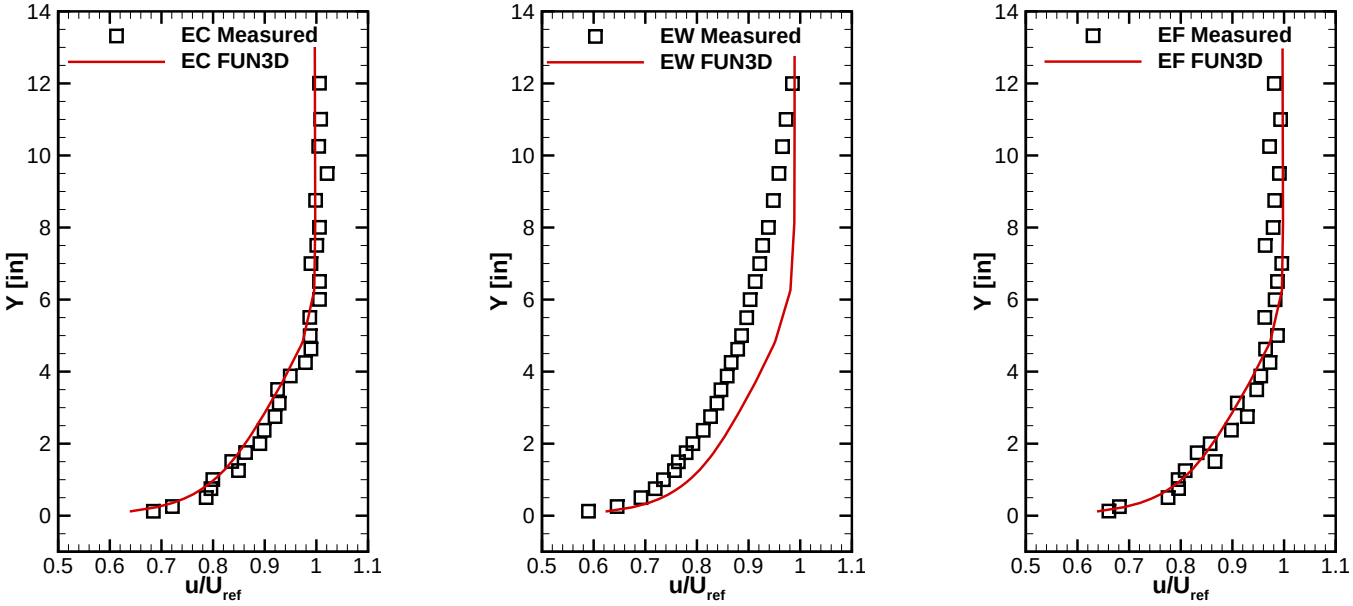

(a) East Ceiling.

(b) East Wall.

(c) East Floor.

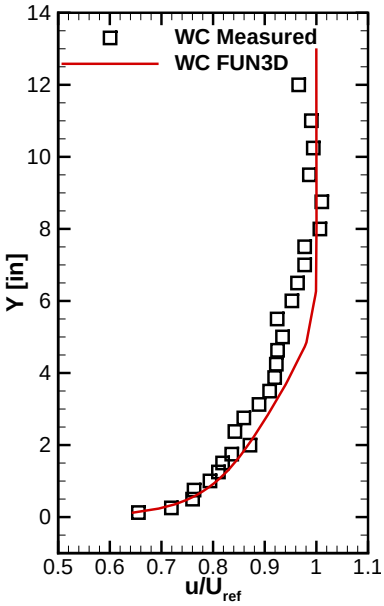

(d) West Ceiling.

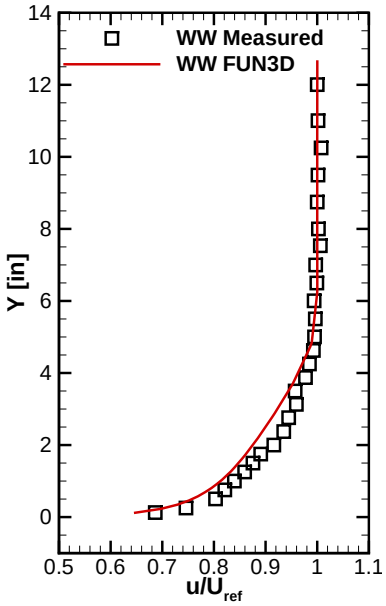

(e) West Wall.

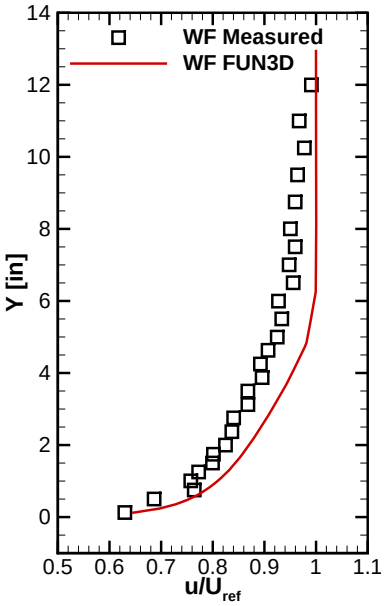

(f) West Floor.

Fig. 8. Measured (Ref. 31) and computed FUN3D boundary layer profiles at the X=72 ft station for the empty TDT running R-134a heavy gas at M=0.2.

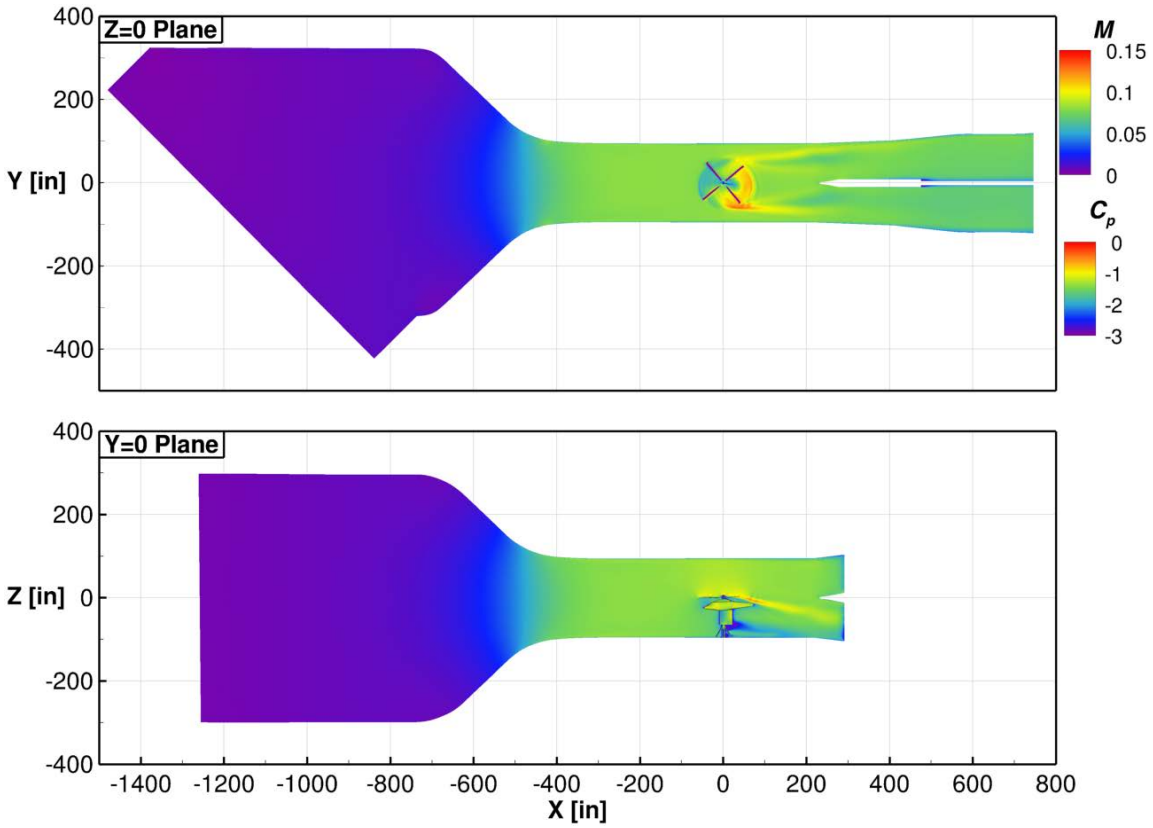

Fig. 9. Cutting planes showing Mach number with ARES/ATR model surfaces colored by C_p for the M=0.08, μ=13 case.

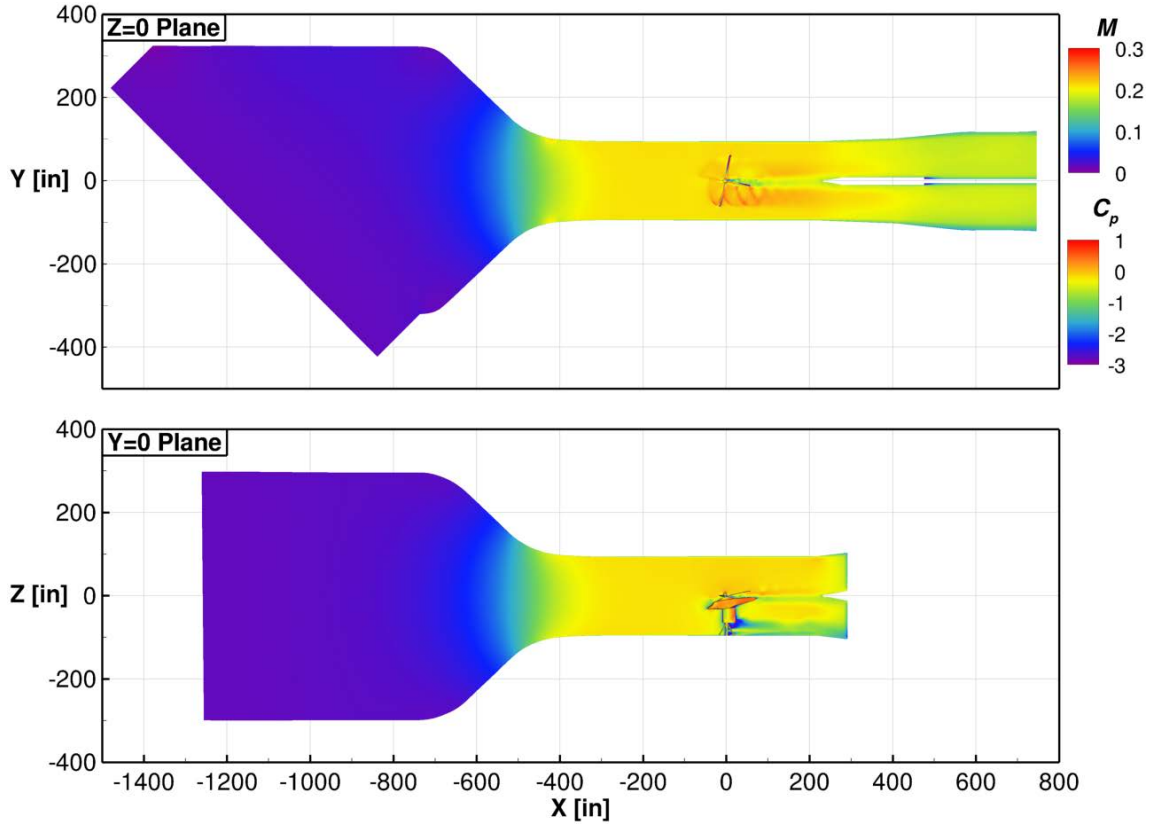

Fig. 10. Cutting planes showing Mach number with ARES/ATR model surfaces colored by C_p for the M=0.21, μ=0.33 case.

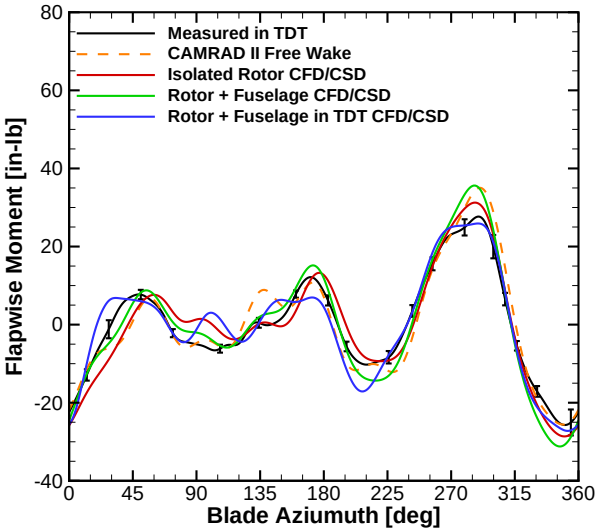

(a) M_β at $r = 0.76$ for $\mu = 0.13$.

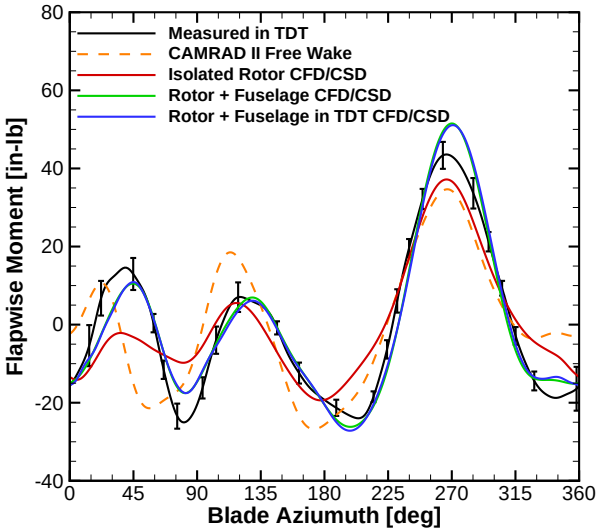

(b) M_β at $r = 0.76$ for $\mu = 0.33$.

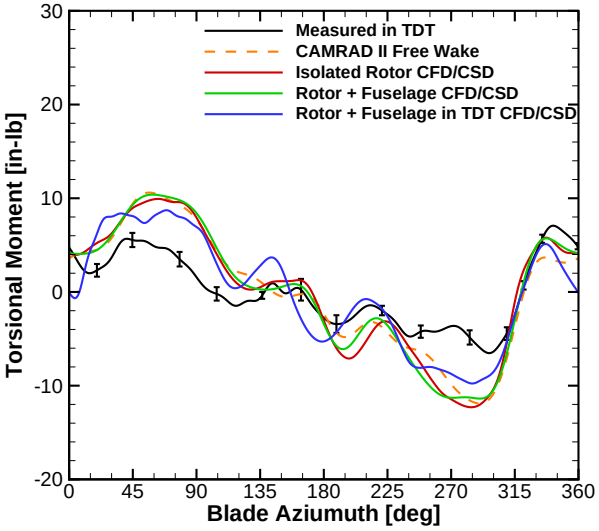

(c) M_θ at $r = 0.24$ for $\mu = 0.13$.

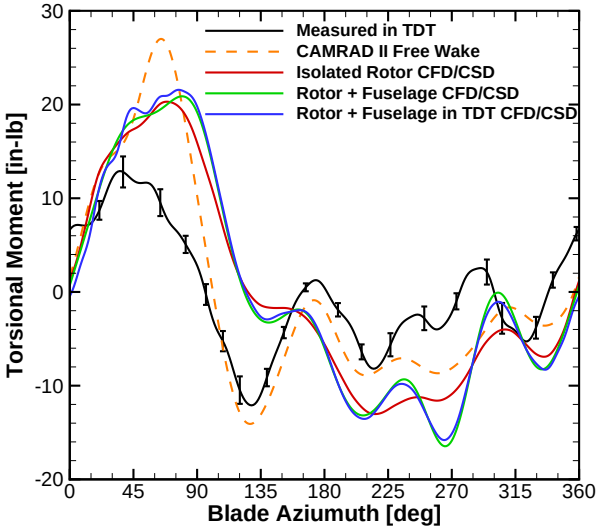

(d) M_θ at $r = 0.24$ for $\mu = 0.33$.

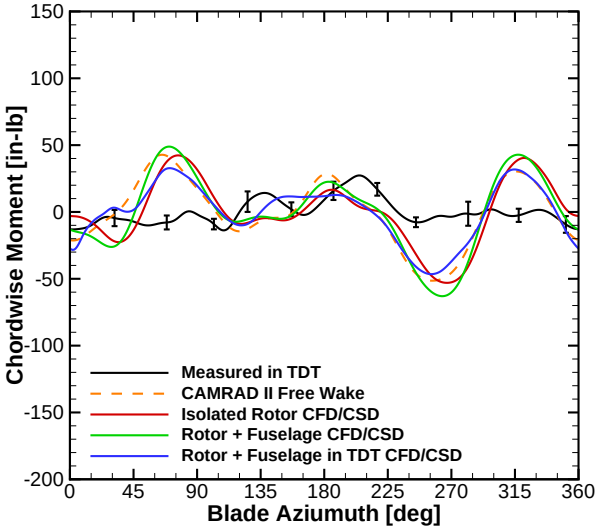

(e) M_ξ at $r = 0.20$ for $\mu = 0.13$.

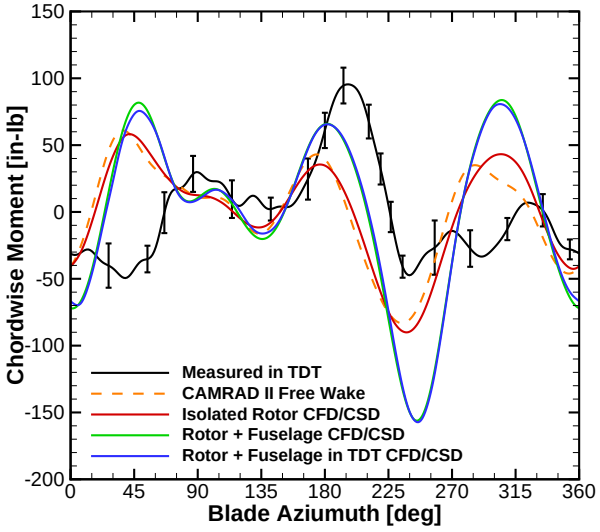

(f) M_ξ at $r = 0.20$ for $\mu = 0.33$.

Fig. 11. Bending moments (mean removed).

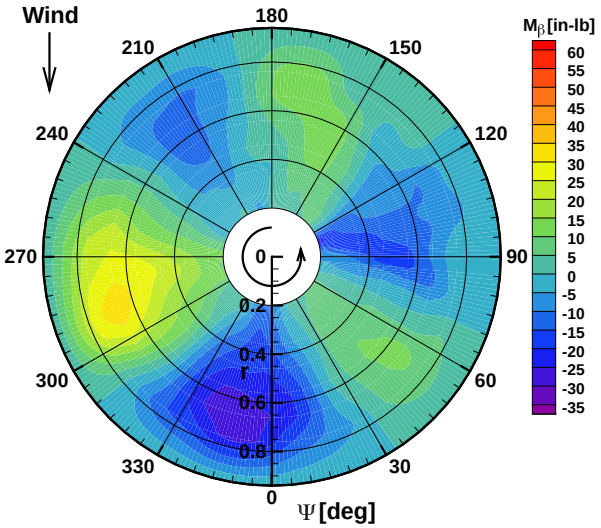

(a) Measured in TDT

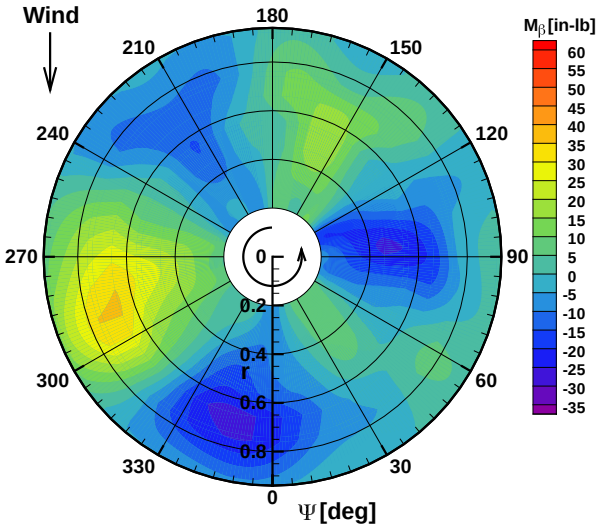

(b) CAMRAD II Free Wake

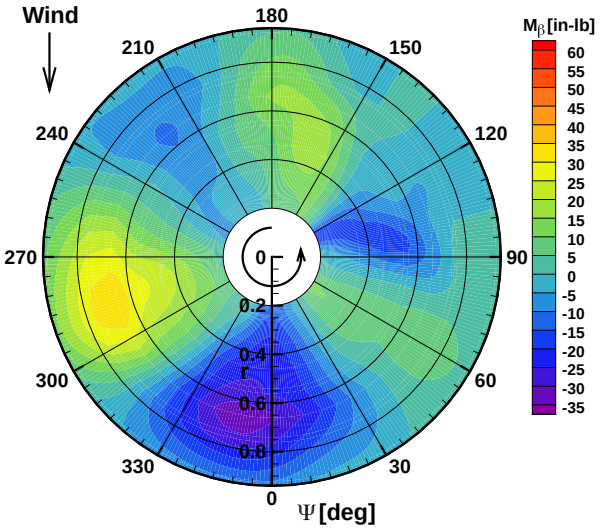

(c) Isolated Rotor CFD/CSD

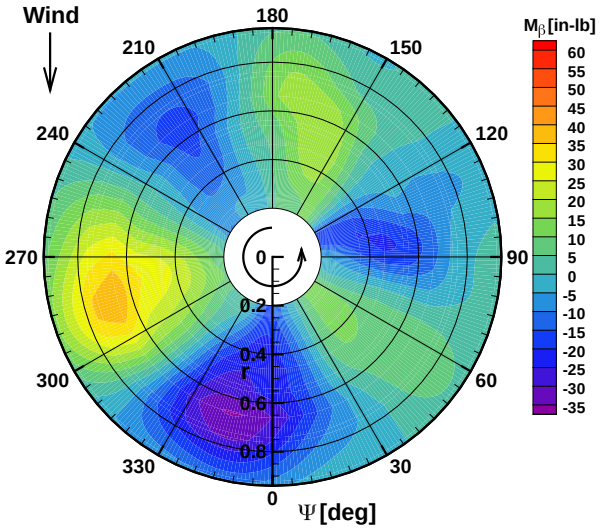

(d) Rotor + Fuselage CFD/CSD

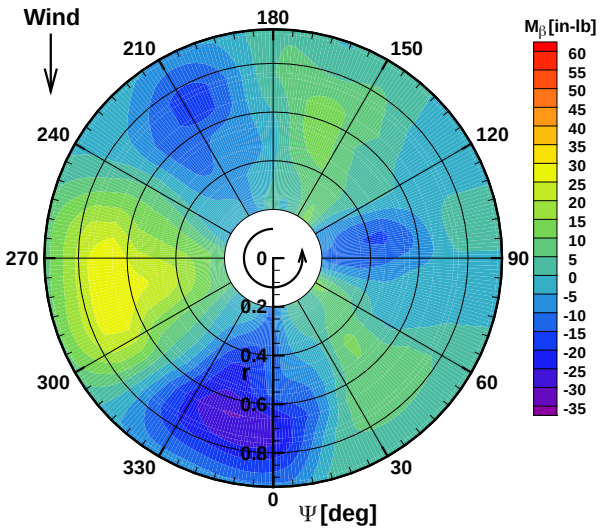

(e) Rotor + Fuselage in TDT CFD/CSD

Fig. 12. Flapwise bending moment (mean removed) for $\mu = 0.13$.

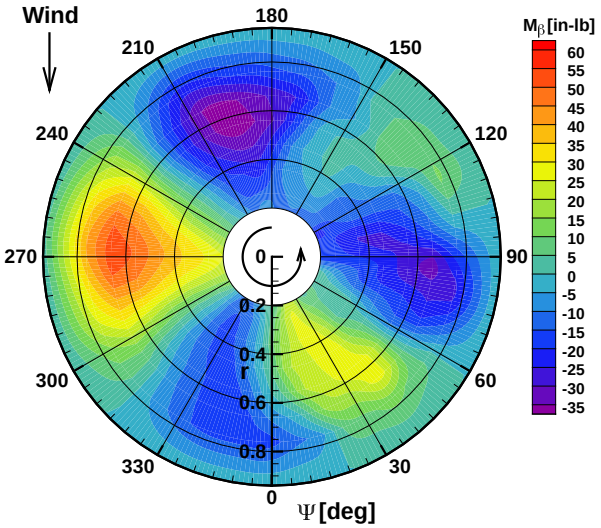

(a) Measured in TDT

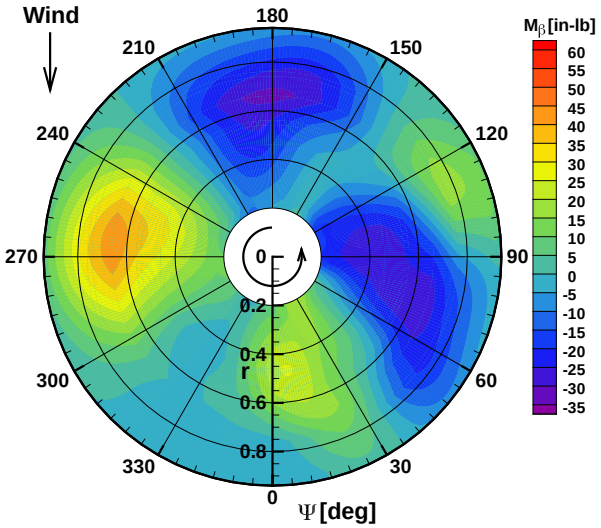

(b) CAMRAD II Free Wake

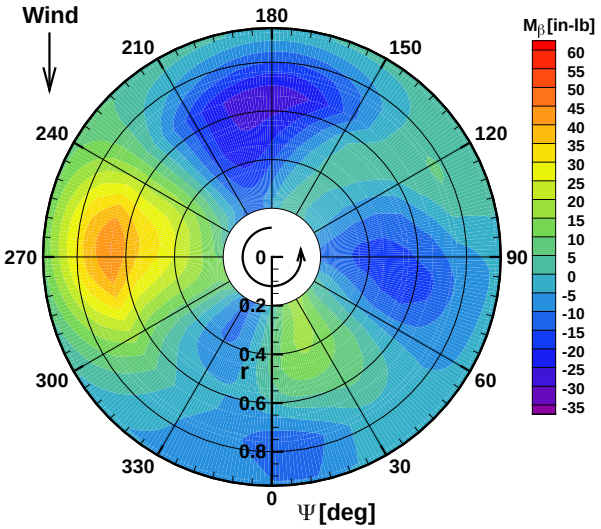

(c) Isolated Rotor CFD/CSD

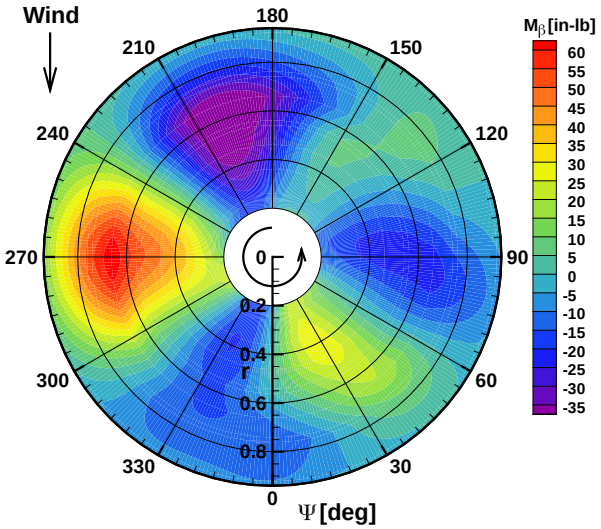

(d) Rotor + Fuselage CFD/CSD

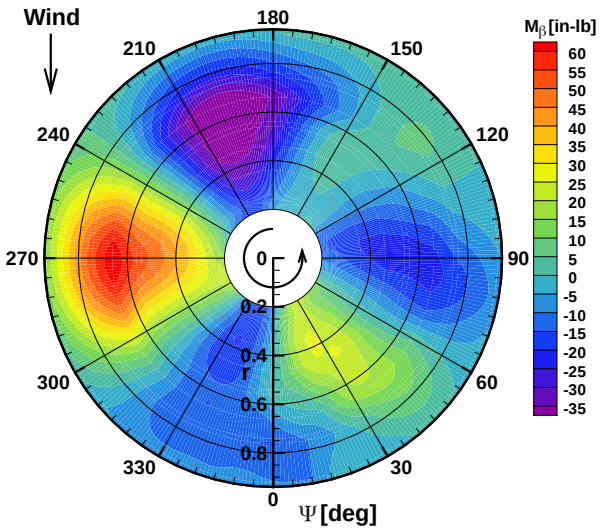

(e) Rotor + Fuselage in TDT CFD/CSD

Fig. 13. Flapwise bending moment (mean removed) for $\mu = 0.33$.

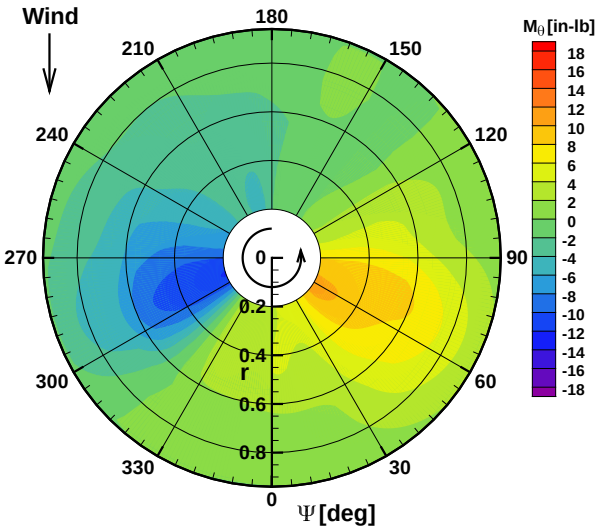

(a) CAMRAD II Free Wake

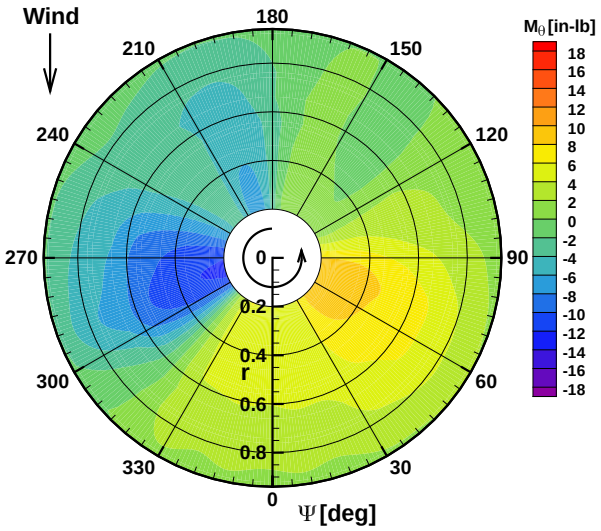

(b) Isolated Rotor CFD/CSD

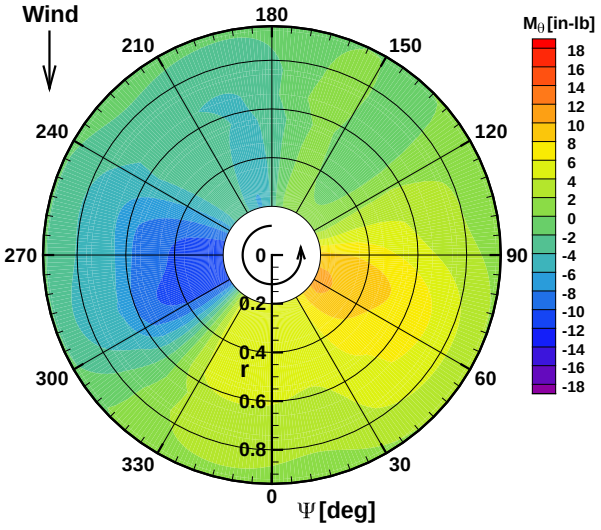

(c) Rotor + Fuselage CFD/CSD

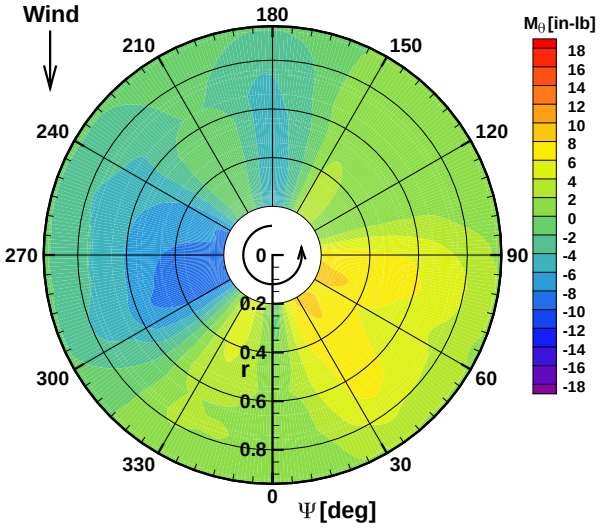

(d) Rotor + Fuselage in TDT CFD/CSD

Fig. 14. Torsional bending moment (mean removed) for $\mu = 0.13$.

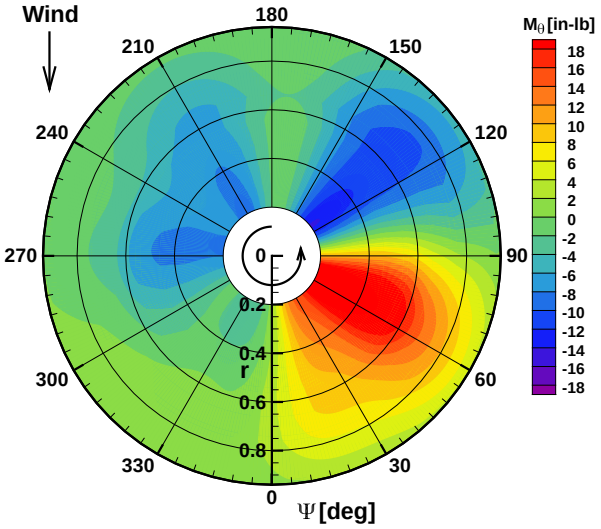

(a) CAMRAD II Free Wake

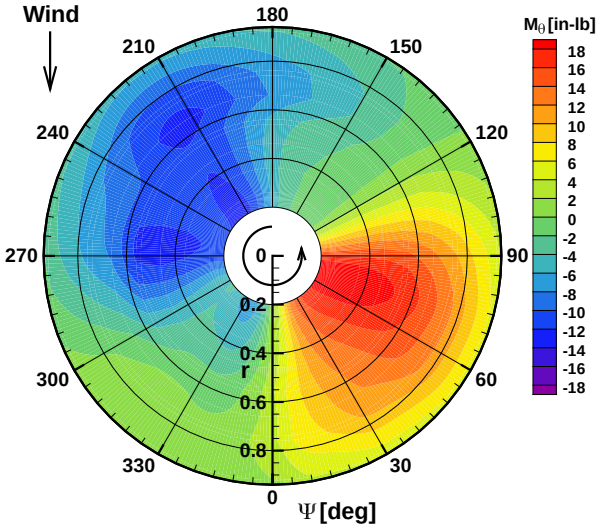

(b) Isolated Rotor CFD/CSD

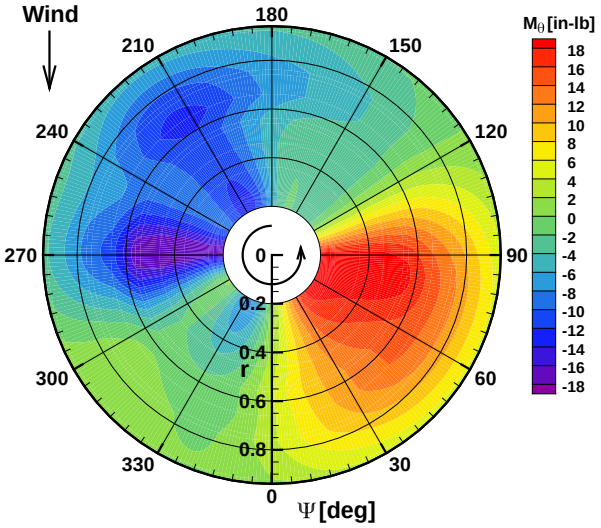

(c) Rotor + Fuselage CFD/CSD

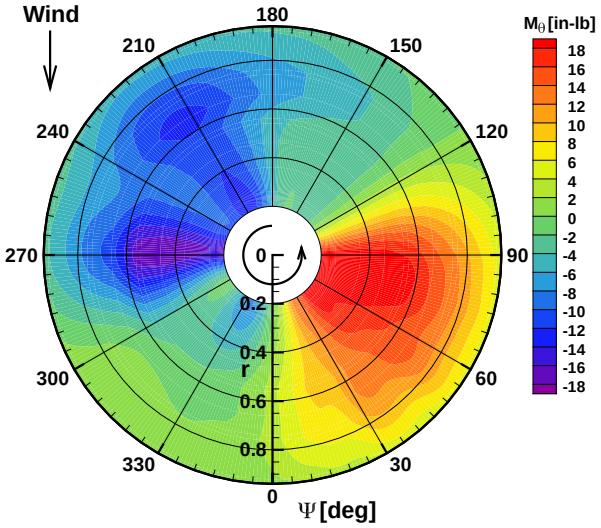

(d) Rotor + Fuselage in TDT CFD/CSD

Fig. 15. Torsional bending moment (mean removed) for $\mu = 0.33$.

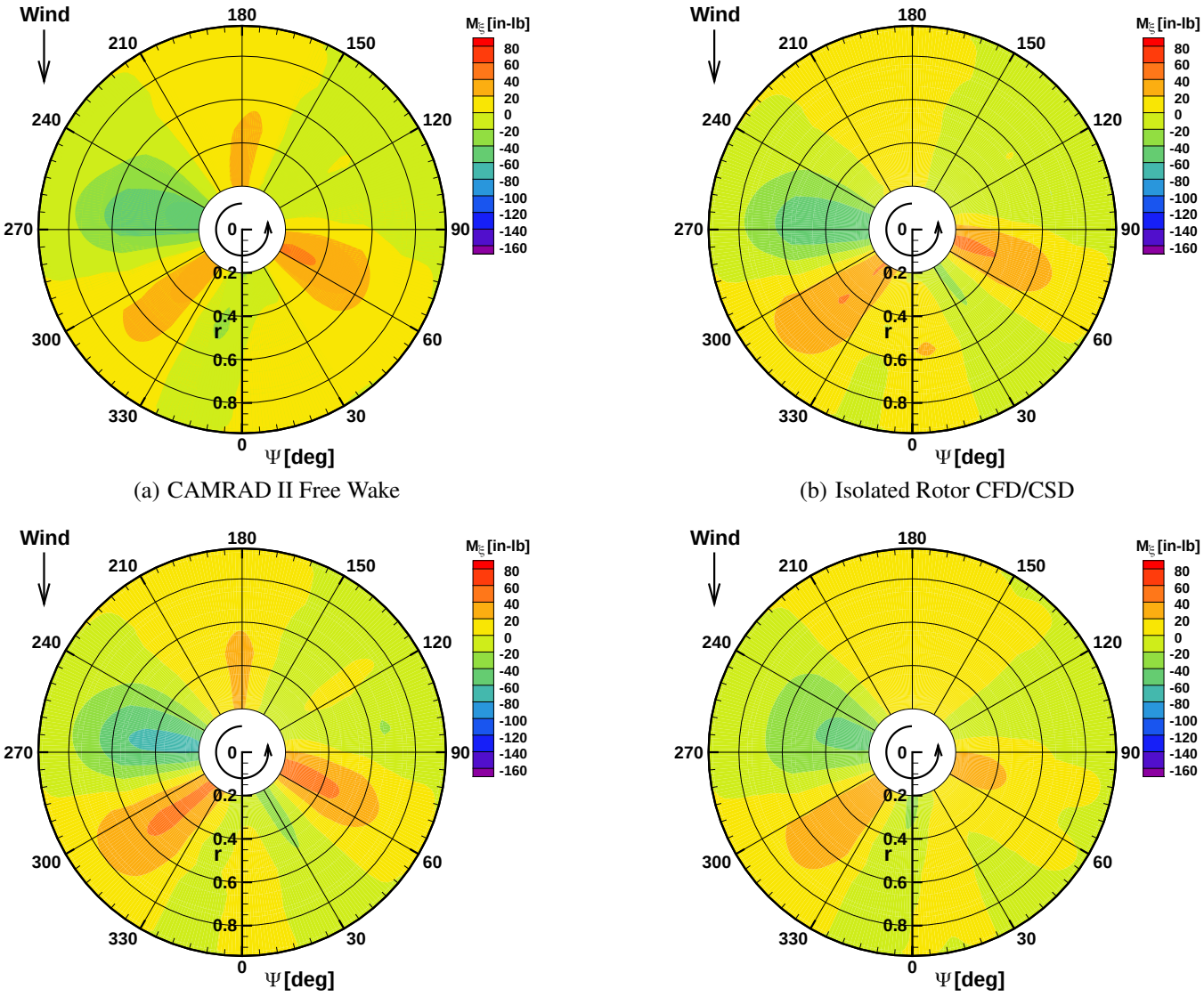

(a) CAMRAD II Free Wake

(b) Isolated Rotor CFD/CSD

(c) Rotor + Fuselage CFD/CSD

(d) Rotor + Fuselage in TDT CFD/CSD

Fig. 16. Chordwise bending moment (mean removed) for $\mu = 0.13$.

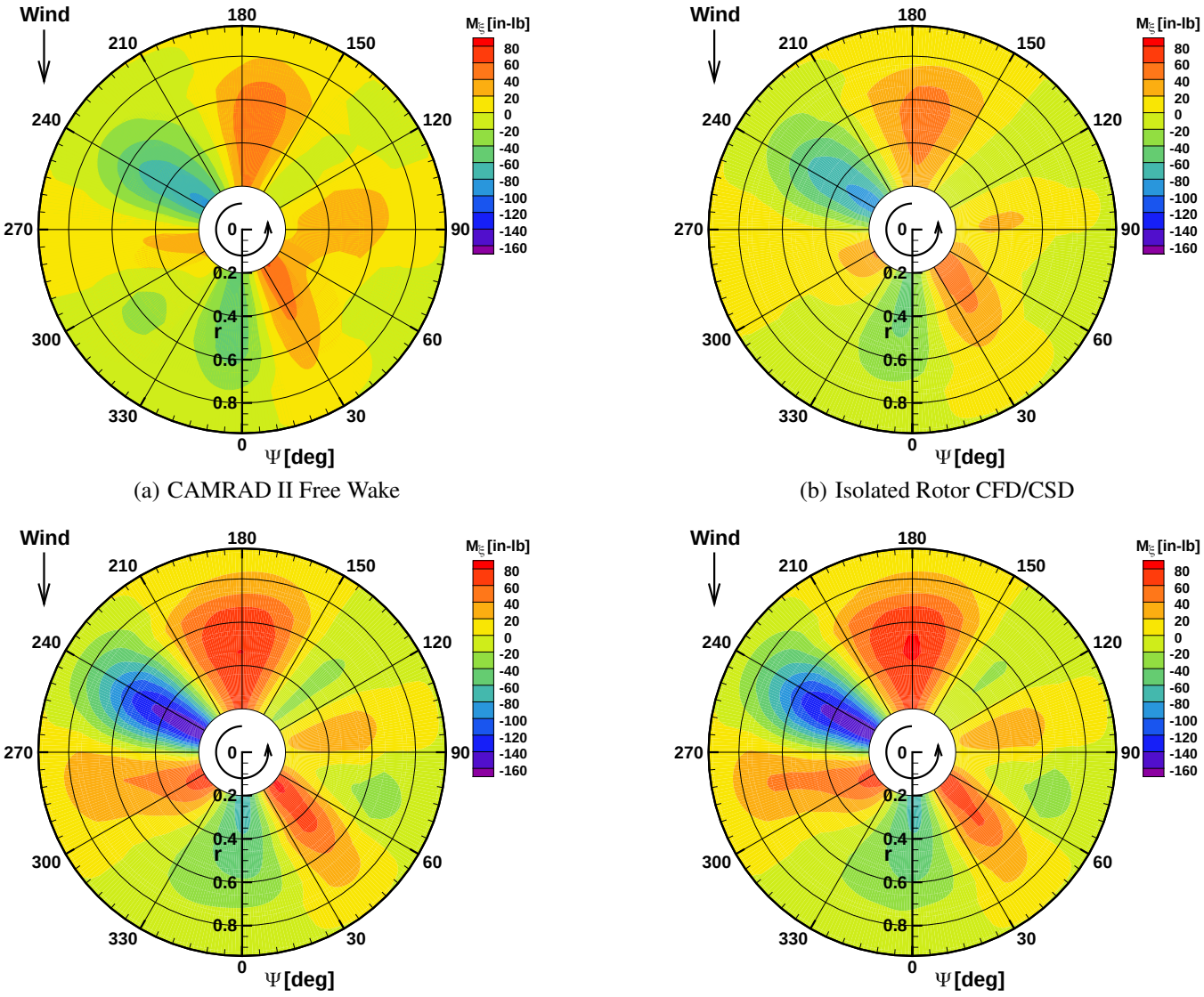

(a) CAMRAD II Free Wake

(b) Isolated Rotor CFD/CSD

(c) Rotor + Fuselage CFD/CSD

(d) Rotor + Fuselage in TDT CFD/CSD

Fig. 17. Chordwise bending moment (mean removed) for $\mu = 0.33$.

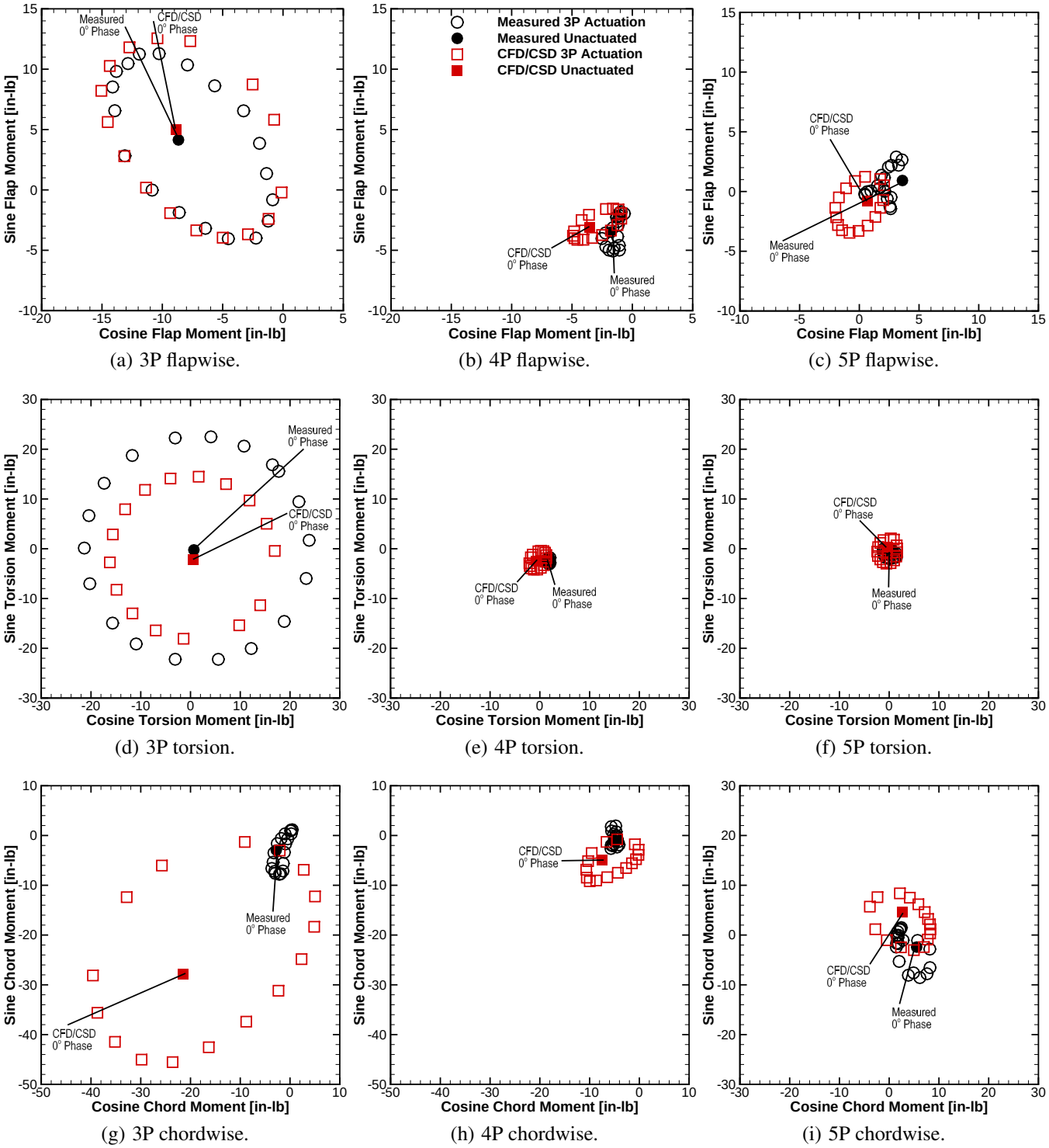

(a) 3P flapwise. (b) 4P flapwise. (c) 5P flapwise.

(d) 3P torsion. (e) 4P torsion. (f) 5P torsion.

(g) 3P chordwise. (h) 4P chordwise. (i) 5P chordwise.

Fig. 18. Effect of 3P actuation on blade loads for $\mu = 0.125$.

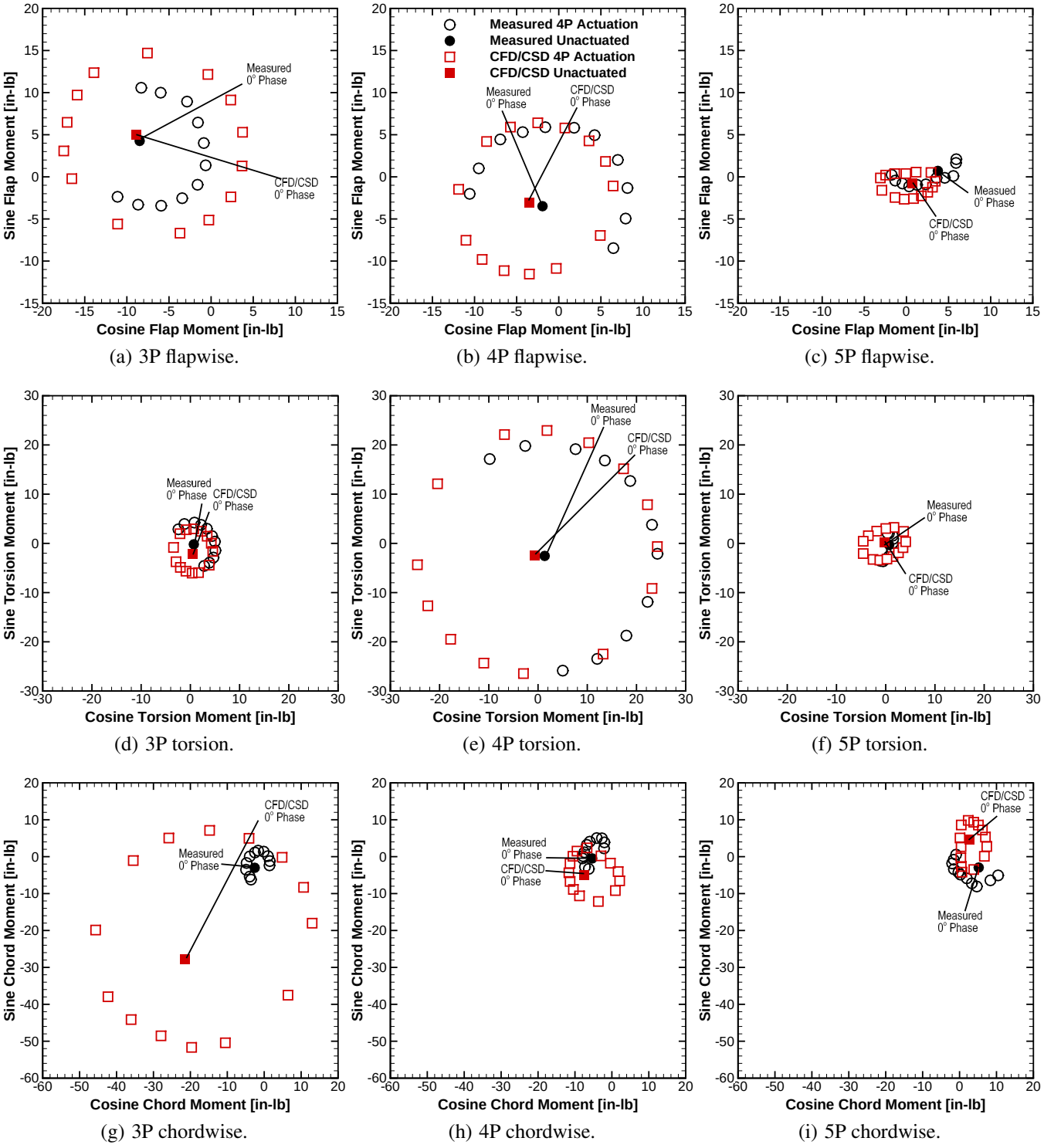

(a) 3P flapwise. (b) 4P flapwise. (c) 5P flapwise.

(d) 3P torsion. (e) 4P torsion. (f) 5P torsion.

(g) 3P chordwise. (h) 4P chordwise. (i) 5P chordwise.

Fig. 19. Effect of 4P actuation on blade loads for $\mu = 0.125$.

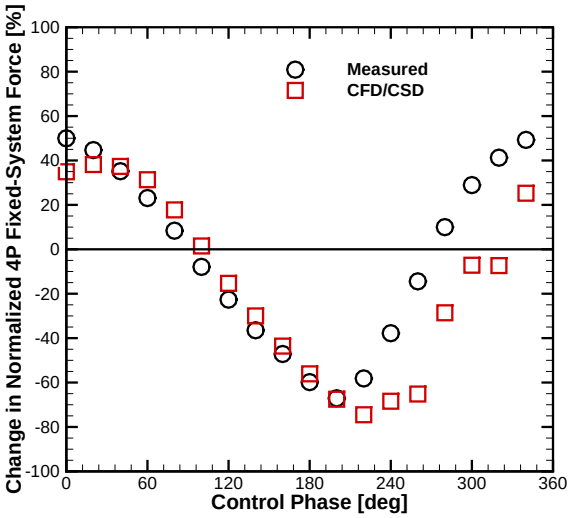

(a) Axial force.

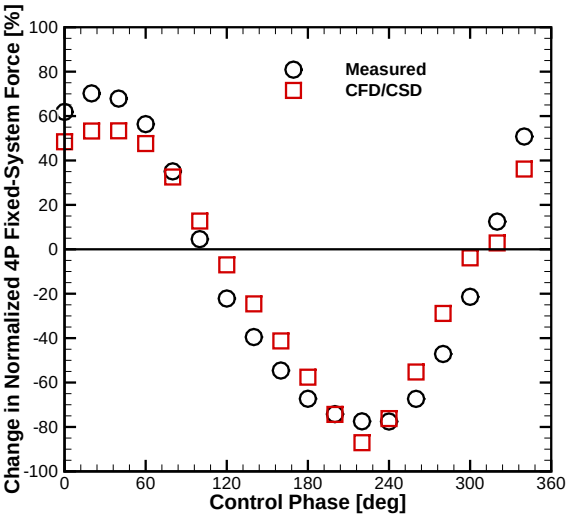

(b) Side force.

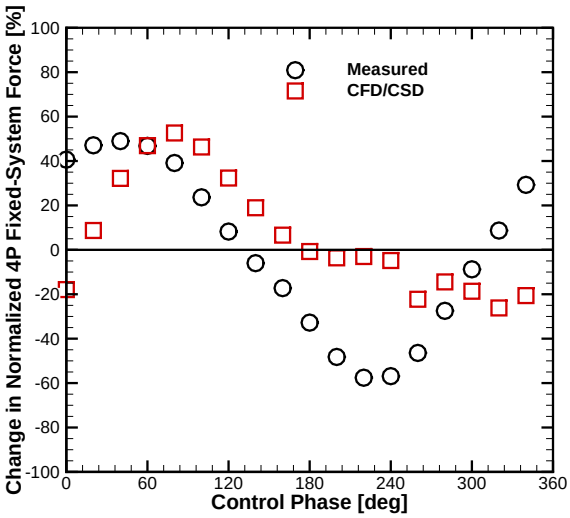

(c) Normal force.

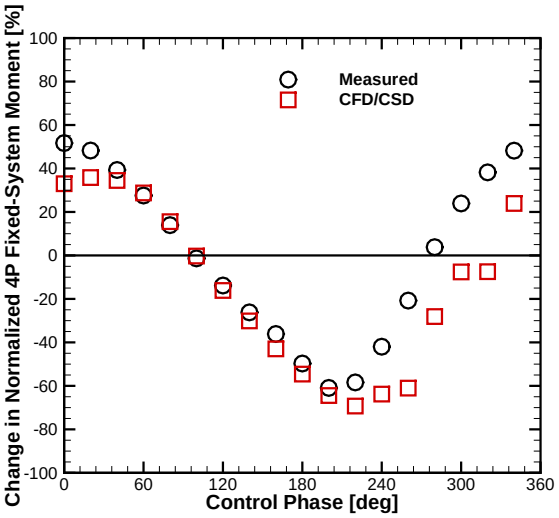

(d) Pitching moment.

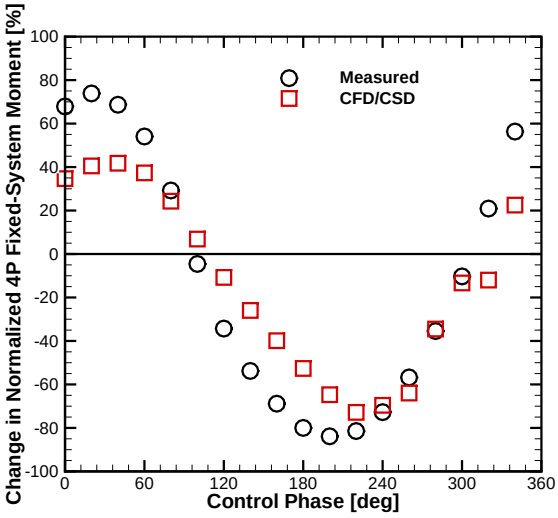

(e) Rolling moment.

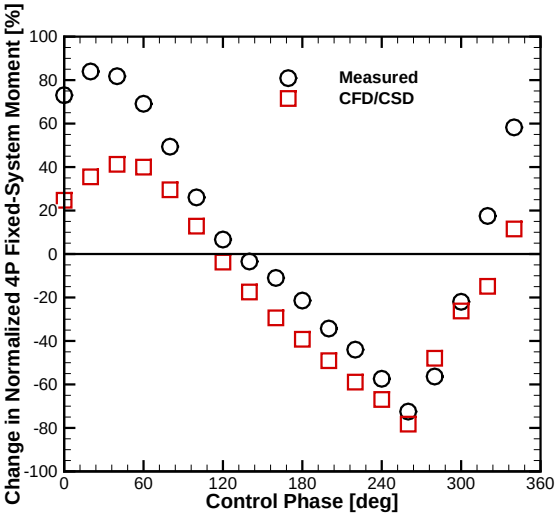

(f) Yawing moment.

Fig. 20. 4P fixed-system loads for $\mu = 0.125$, 3P actuation at 500 V.